Article:
Abul, M. R., Cochrane, R. F., Mullis, A. M. orcid.org/0000-0002-5215-9959 et al. (1 more author) (2024) Microstructural Evolution and Mechanical Properties of Drop Tube Processed Al-4.1 Wt% Fe-1.9 Wt% Si. Journal of Materials Engineering and Performance, 33. pp. 8840-8856. ISSN 1059-9495

https://doi.org/10.1007/s11665-023-08561-6

Microstructural Evolution and Mechanical Properties of Drop Tube Processed Al-4.1 wt% Fe-1.9 wt% Si

Mehmet R. Abul [*, 1], *Robert F. Cochrane* [2], *Andrew M. Mullis* [2] *& Ahmed Nassar* [2]

[*] Corresponding author

email: mrabul@aybu.edu.tr

phone: 90 507 252 80 48

[1] Ankara Yildirim Beyazit University, Kecioren, Ankara, Turkey

[2] School of Chemical & Process Engineering, University of Leeds, Leeds LS2 9JT, UK

Abstract

The microstructural evolution of drop-tube processed Al-4.1wt% Fe-1.9 wt% Si alloy powders has been analysed. X-ray diffraction shows that, irrespective of the cooling rate, the only intermetallic formed is Al_8Fe_2Si. Microstructural analysis reveals that the larger powders (d > 300 µm) comprise a mixed microstructure comprising microcellular and dendritic regions with a lamellar interdendritic eutectic. Smaller powders tend to also contain one or more featureless faceted regions, the prevalence of which increases with decreasing sample size. In the smallest powder sizes (d < 106 µm), propeller-like structures with either 3- or 4-arms were observed to be formed from the same featureless material due to a change in the growth mechanism from faceted to continuous. The Fe content of the featureless material was found to be same as the melt, while the Si content was measured as 1 wt% Si. TEM analysis reveals that this "featureless" material comprises clusters of nano-sized faceted Al_8Fe_2Si crystals in an α-Al matrix. It seems likely that this material formed as a result of partitionless solidification with respect to Fe, with the resulting highly supersaturated solid-solution subsequently undergoing decomposition forming nano-crystalline Al_8Fe_2Si. The microhardness of the samples increased from 72 $HV_{0.01}$ to 90 $HV_{0.01}$ as the sample size was decreased from 850 µm to 150 µm but later dropped from 90 $HV_{0.01}$ to 80 $HV_{0.01}$ for 150 µm to 53 µm samples, respectively. The nanohardness of angular region was measured as 1.76 ± 0.04 GPa, that of dendritic region was measured as 1.3 ± 0.09 GPa.

Key words: Al-Fe-Si alloys, non-equilibrium solidification, faceted growth, partitionless solidification, solid-state decomposition, nanohardness

1. Introduction

Al alloys are of interest for their low density, excellent corrosion resistance and high specific modulus. However, such alloys can include considerable amounts of both Fe and Si, either as alloying elements or as difficult to remove impurities(Zhang et al. 2012). As the solid solubility of both Fe and Si is very low in α-Al, these elements form binary Al-Fe and/or ternary Al-Fe-Si phases. In the Al rich part of the ternary Al-Fe-Si system a number of binary and ternary intermetallics have been reported. The binary Al-Fe phases include the equilibrium $Al_{13}Fe_4$ phase, Al_6Fe(Hu, Yu, and Le 2020), Al_mFe(Young and Clyne 1981), Al_xFe(Chen et al. 2013) and Al_9Fe_2(Simensen, C. J., & Vellasamy 1977), while the ternary Al-Fe-Si phases include α-Al_8Fe_2Si, β-Al_5FeSi and δ-Al_4FeSi_2(Ahmed and Ebrahim 2014; Griger and Stefaniay 1996; Khalifa, Samuel, and Gruzleski 2003; Kiliçaslan et al. 2013). Which of these intermetallic compounds are observed to form is a function of both the Fe:Si ratio as well as the cooling rate. While low cooling rates and high Fe:Si ratio promote the formation of the binary Al-Fe phases, high cooling rates and low Fe:Si ratio nurture the formation of the ternary Al-Fe-Si phases(Griger and Stefaniay 1996).

In this paper, an Al-4.1 wt% Fe-1.9 wt% Si alloy will be considered, the equilibrium solidification path for which (**Figure 1**) starts with the formation of primary $Al_{13}Fe_4$, with upon further cooling the formation of α-Al below 650 °C. Finally, a peritectic reaction takes place at 632 °C forming ternary Al_8Fe_2Si intermetallic.

Rapid solidification (RS) processing promises remarkable microstructural and constitutional changes in various alloy systems. RS can be achieved by different methods. Among the present techniques, drop-tube processing which combines both high cooling rates and, thanks to its containerless nature, deep undercooling, remains as a leading RS technique. Solidification takes place during free fall in the drop-tube, eliminating many possible heterogeneous nucleation sites that would otherwise arise due to contact with the container walls(Li et al. 2009; Mullis, Bigg, and Adkins 2015).

The ternary Al-Fe-Si alloy system has been investigated with varying solute content and various cooling rates. (Khalifa et al. 2003) studied rather dilute alloys with Fe content below 1 wt% and Si composition up to 6 wt% using mould casting with cooling rates changing from 0.16 K s^{-1} to 15 K s^{-1}. They observed binary Al-Fe intermetallics for cooling rates below 0.19 K s^{-1}, with cooling rates higher than this promoting the ternary intermetallics. Moreover, while ternary β-Al_5FeSi was dominant at relatively low cooling rates, raising the cooling rate led to

the evolution of a mixed α-Al_8Fe_2Si + β-Al_5FeSi microstructure. Similar findings were also outlined by (Zhang et al. 2009), who found $Al_{13}Fe_4$ is replaced by α-Al_8Fe_2Si with increasing cooling rates up to 100 K s^{-1} in Al-14 wt% Fe-2 wt% Si alloy. Furthermore, irregular α-Al_8Fe_2Si transitioned into more regular (lamellar) structures with increasing cooling rate.

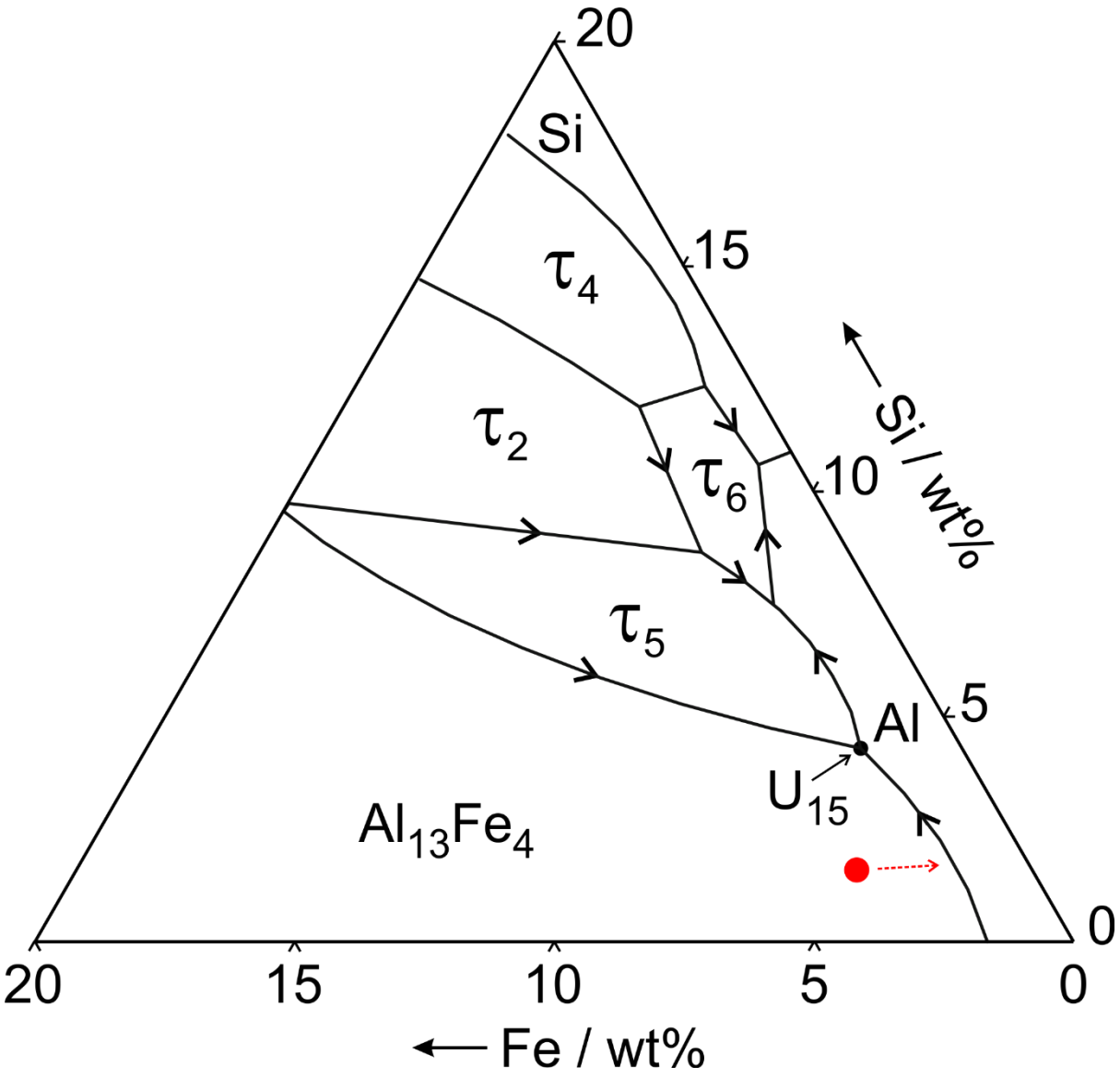

Figure 1: Liquidus projection for the Al-rich corner of the ternary Al-Fe-Si system (redrawn after(Du et al. 2008)). The composition of the alloy used in this work is shown by the dot, with the initial equilibrium solidification path shown by the dashed line. Note that the notation of Du et al. is used on the diagram wherein the common ternary intermetallics are denoted as τ_5 = α-Al_8Fe_2Si, τ_6 = β-Al_5FeSi and τ_4 = δ-Al_4FeSi_2.

There are several studies on Fe and Si bearing ternary Al systems with cooling rates as high as 10^5 K s^{-1} using melt spinning. (Ünlü et al. 2001) studied Al-3.3 wt% Fe-10 wt% Si and Al-3.3 wt% Fe-20 wt% Si alloys. They did not report the presence of either binary or ternary intermetallics. Only α-Al was present in the former alloy, while in the latter alloy nano-sized

spherical Si particles were found due to the higher concentration of Si. Similarly, (Kiliçaslan et al. 2013) and (Ahmed and Ebrahim 2014) have observed the evolution of nanosized Si particles after melt spinning Al-5 wt% Fe-25 wt% Si and Al-11 wt% Fe-11 wt% Si alloys, respectively. They also reported a metastable extension of the Si solubility in α-Al up to 1 wt% Si. In addition to nano-sized Si particles, ternary β-Al_5FeSi and δ-Al_4FeSi_2 were formed due to the high iron concentration.

The purpose of this study is to investigate the effect of cooling rate on the microstructural development of drop-tube processed Al-4.1 wt% Fe-1.9 wt% Si by employing X-ray diffraction (XRD), optical microscopy (OM), Scanning Electron Microscopy (SEM) and Transmission Electron Microscopy (TEM) techniques. Moreover, the mechanical properties of the rapidly solidified samples were analysed utilizing microhardness and nano-indentation techniques.

2. Experimental Procedure

The Al-4.1 wt% Fe-1.9 wt% Si master alloy was made utilizing high purity (>99.9 wt%) Al, fine high purity (>99.9 wt%) Fe wire and high purity (>99.99 wt%) Si lump. These were put in an arc-furnace and the furnace evacuated to a pressure of 5 x 10^{-4} Pa. The furnace was then backfilled with Argon to a pressure of 3.4 x 10^3 Pa. The evacuation and backfilling were repeated 5 times to flush the system and ensure a low oxygen environment for melting. The master alloy was melted five times using the arc-furnace and between each melting cycle the alloy was turned over in order to verify thorough mixing of the constituent elements. The sample was then mounted, polished and analysed under XRD, OM and SEM to verify the homogeneity of the resulting master alloy. After confirmation of complete mixing, the master alloy was atomized using a 6.5 m drop-tube details of which are provided elsewhere(Abul, Cochrane, and Mullis 2022a).

The drop-tube processing produced spherical powders which were collected and sieved in to following sieve fractions: 850-500 µm (145 K s^{-1}), 500-300 µm (350 K s^{-1}), 300-212 µm (750 K s^{-1}), 212-150 µm (1360 K s^{-1}), 150 -106 µm (2450 K s^{-1}), 106-75 µm (4430 K s^{-1}) and 75-53 µm (8000 K s^{-1}), with the quoted cooling rates being given by the balance of heat flow for a droplet in the middle of the size range. The method is described in detail in (Abul et al. 2022a).

X-ray diffraction was carried out on each size fractions using a Bruker D8 Diffractometer with Cu K_α radiation between 2θ values of 20° to 80° with a step size of 0.033°. Peak indexing and phase identification was performed using the Malvern Panalytical HighScore software. The

samples were then hot mounted in Bakelite for microscopic examination and the samples were ground using 800, 1200, 2000 and 2500 grit SiC papers progressively. Polishing was then performed using 6 µm, 3 µm and 1 µm diamond pastes. The final polishing was employed on a semiautomatic polisher utilising 0.05 µm colloidal silica solution for 90 seconds to obtain scratch free surface. To eliminate the contamination, the samples were washed water and methanol after grinding and polishing. Etching was performed with Keller's Reagent (1% HF, 1.5 % HCl, 2.5% HNO_3 and 95% water). Optical microscopy was performed using an Olympus BX51 optical microscope.

After optical microscopy, the polished samples were carbon coated for SEM analysis. A Hitachi Su8230 SEM equipped with built in energy dispersive X-ray analyser (EDS) was used. FEI nova 200 NanoLab FEGSEM with a built-in Focused Ion Beam (FIB) was utilized to section samples for Transmission Electron Microscopy (TEM) analysis. The FIB cut samples were later analysed utilizing an FEI Titan3 Themis 300 TEM.

Microhardness measurements were carried out utilizing a Tukon^{TM} 1202 Wilson Hardness (Vickers) tester on colloidal silica polished samples at room temperature, using 10g load. The measurement was repeated 10 times for each sample size. Moreover, nano indentation studies using a Micro Materials Ltd. NanoTest machine were performed on two samples from the 75-53 µm size fraction to reveal the differences in the mechanical properties of different regions within the powder microstructure. The sample was briefly etched using Keller's reagent for one second to distinguish the angular and dendritic zones. The load for the nanohardness measurements was set as 15 mN and 20 mN, respectively.

Eutectic spacing was measured using ImageJ software to draw lines of length, v, perpendicular to the eutectic lamellar on SEM images of the eutectic microstructure. The number of lamellae, c, was then ascertained and the lamellar spacing, λ, determined by:

$$\lambda = v/c \tag{1}$$

3. Results

3.1 XRD results

XRD results for the arc-furnace prepared master alloy and selected drop-tube atomized size fractions are provided in **Figure 2**. Both figures show the presence of the same phases, namely α-Al and Al_8Fe_2Si. That is, despite the various cooling rates experienced by the samples, the phases in both the master alloy and the drop-tube samples do not change and are limited to just

the one ternary intermetallic. However, drop-tube atomized samples with d < 212 µm display two diffraction peaks (indicated with black arrows in **Figure 2b**) 2θ values for which are around 30° and which were not identified using HighScore. These peaks may therefore belong to a metastable phase which has not been able to be identified. The intensity of these two peaks, as seen from **Figure 2b**, is rising with the drop in the sample size, indicating that the metastable phase may be becoming more prevalent with increasing cooling rate.

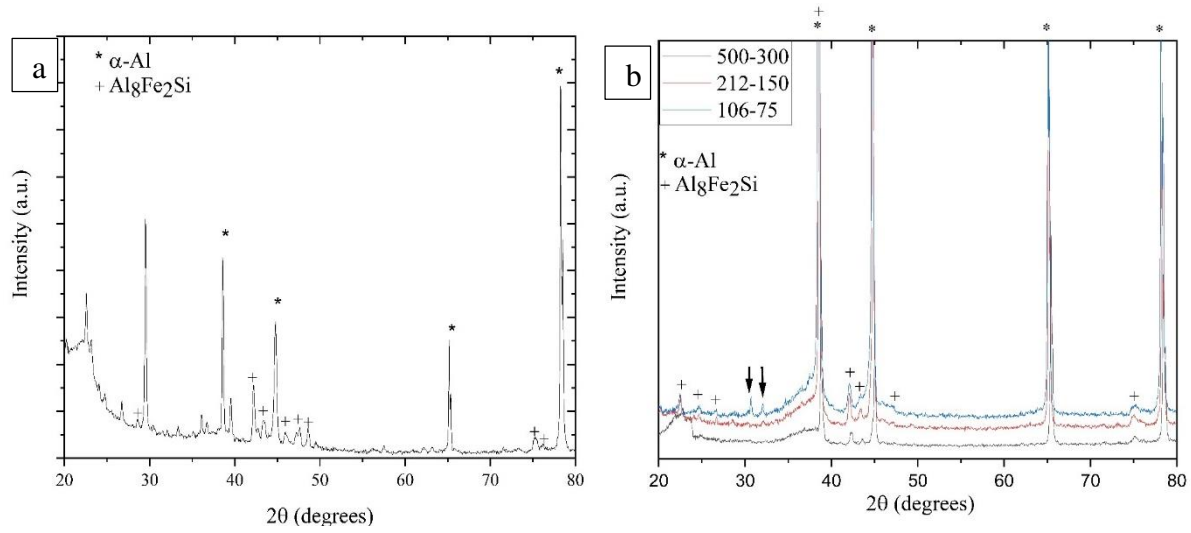

Figure 2: XRD diffraction results of a) the arc-furnace prepared master alloy showing α-Al and Al_8Fe_2Si phases while the unlabelled peaks are from Bakelite and b) the samples with diameters of 500-300 µm, 212-150 µm and 106-75 µm. Arrows indicate two unidentified peaks which increase in intensity as the powder size decreases.

3.2 Microstructure and phase identification

OM and SEM micrographs of the furnace cooled sample are given in **Figure 3**. As seen from **Figure 3a and b**, the microstructure consists of a seaweed-like eutectic in an α-Al matrix. As seen from **Figure 3a and b**, the seaweed structure has branching arms, which are encircled by large script-like, intermetallic. **Figure 3c and d** show SEM images of the same sample displaying eutectic colony formation. A fine rod-like eutectic is formed at the centre of each eutectic colony, with this being surrounded by coarse script-like intermetallics. EDX measurements have been performed on both the α-Al matrix and script-like eutectic. However, the rod-like eutectic is so fine that it is unlikely to get precise EDX composition measurements for the intermetallic phase, due to the electron interaction volume being larger than the rod diameter. Consequently, EDX measurements were not performed on the rod-like phase within the eutectic. The α-Al matrix has been found to contain 0.7-0.8 wt% Si and 0.2- 0.3 wt% Fe, although both solutes have extremely low solubilities in α-Al according to the equilibrium binary phase diagrams. Therefore, it may be concluded that even relatively slow furnace

cooling of the master alloy has extended the solid solubility of both solutes in α-Al. Moreover, the chemical composition of the script-like eutectic has been measured as 72 at.% Al, 18.59 at.% Fe and 9.2 at.% Si, which corresponds closely to that of the Al_8Fe_2Si phase. This is consistent with the XRD data given in **Figure 2a**, which indicated the Al_8Fe_2Si phase as the only intermetallic. Given this it can be assumed that the rod-like intermetallic comprising the eutectic is also Al_8Fe_2Si, but this cannot, as explained above, be confirmed by EDX in the SEM. The rod-like eutectic will later be discussed when TEM results are introduced.

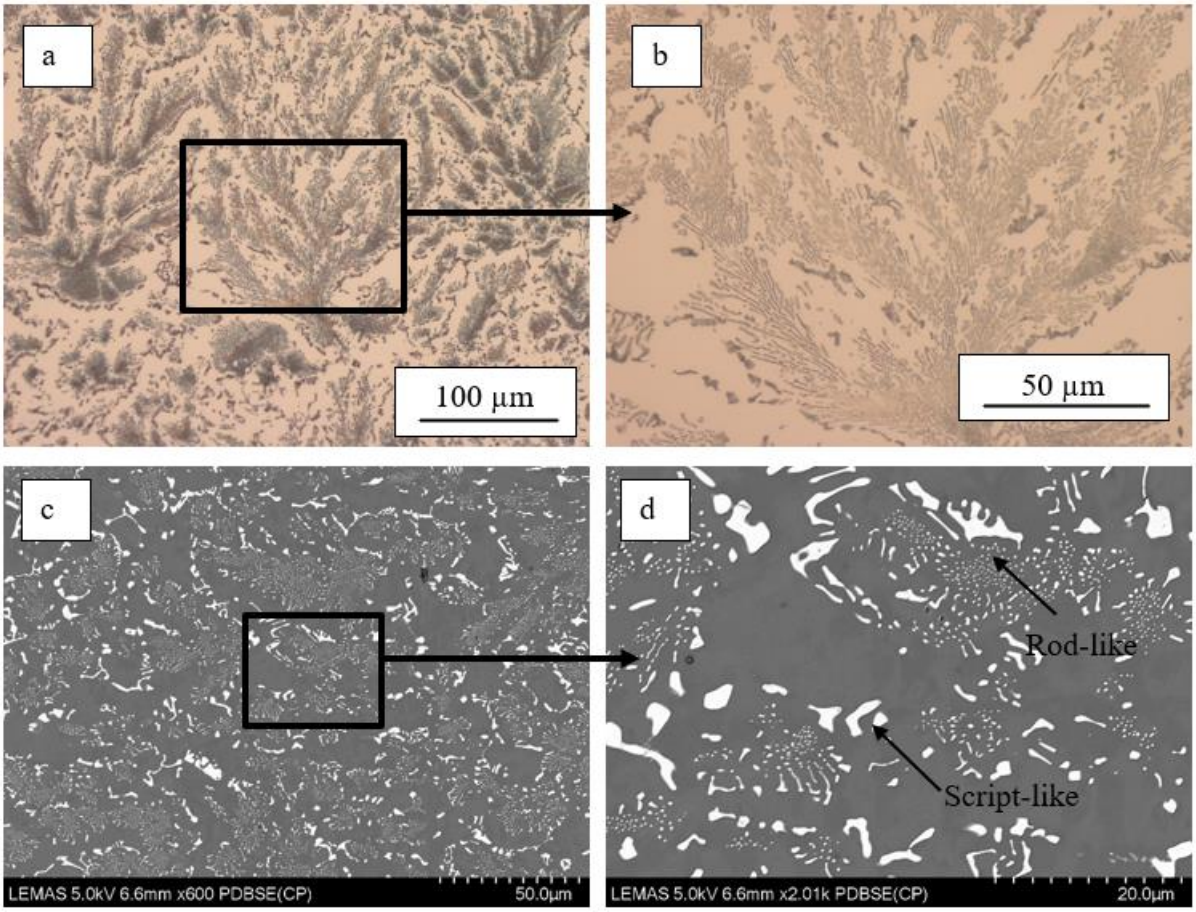

Figure 3: a) and b) OM micrographs of furnace cooled sample depicting seaweed eutectic morphology in an α-Al matrix. c) and d) SEM micrographs of furnace cooled sample exhibiting colonies of rod-like eutectic surrounded by a coarse proeutectic phase.

Figure 4 shows the OM micrographs of the large sieve fractions of the drop-tube atomized samples; namely 850-500 µm and 500-300 µm sieve fractions. The microstructure of these large powders has two well defined regions: microcellular and dendritic regions, with lamellar eutectic between cell boundaries and in the interdendritic region. Considering the extensive appearance of α-Al dendrites, it can be concluded that the first phase to nucleate is α-Al. As the micrograph of furnace cooled sample (**Figure 3c and d**) is completely eutectic, even the

slowest cooling rate of 145 K s^{-1} in the drop-tube has drastically changed the microstructure from a pure eutectic to a dendritic structure with a lamellar interdendritic eutectic (the lamellar interdendritic eutectic being clearly visible in **Figure 5c**). The transition has taken place in the slowest cooled sample with an average estimated cooling rate of 145 K s^{-1}. As seen from **Figure 4d** the lamellar eutectic in the cellular region is coarser than the interdendritic eutectic. Furthermore, dendrite tip splitting is highly pronounced in both samples as labelled in the figure.

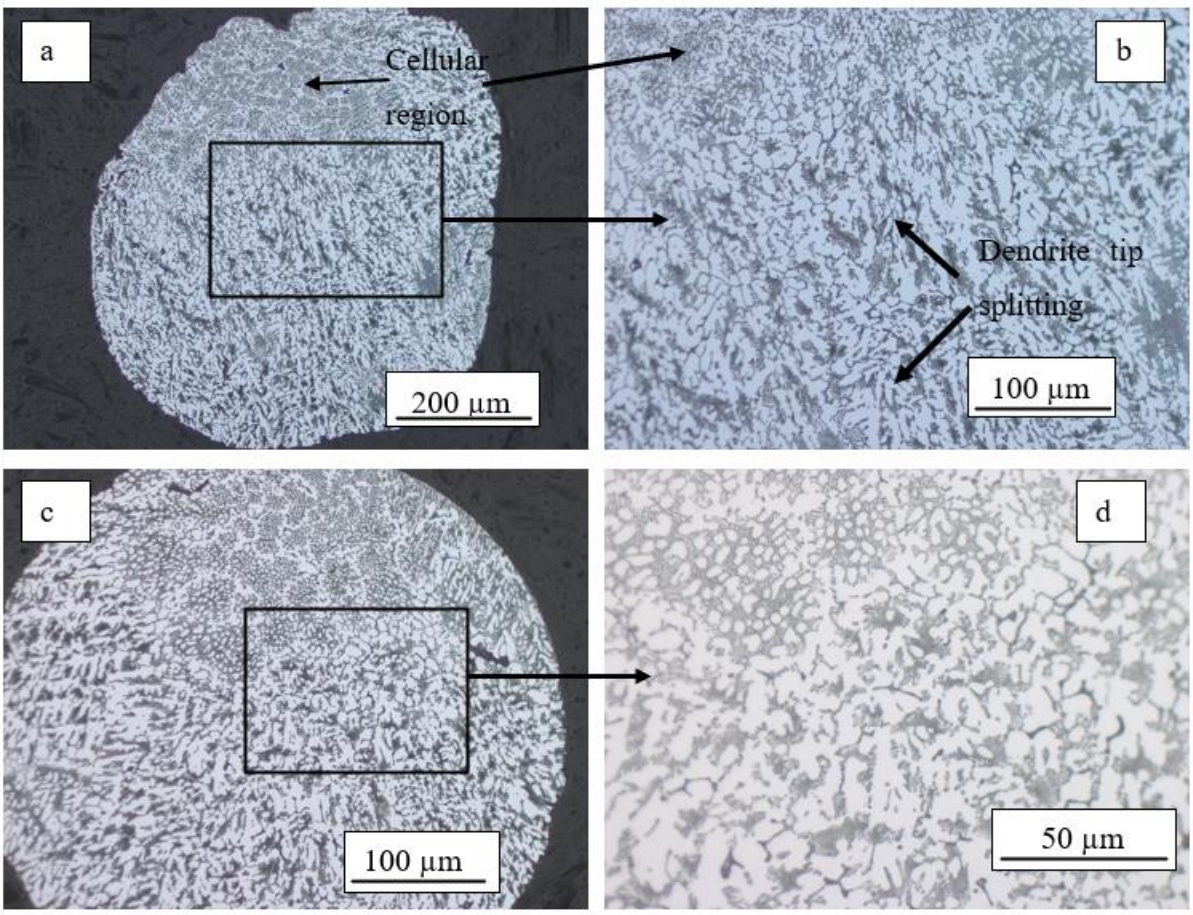

Figure 4: OM images of a) and b) 850-500 µm samples and c) and d) 500-300 µm samples showing the microstructure is microcellular and dendritic with lamellar interdendritic eutectic.

Although most of the 300-212 µm samples share a similar microstructure with the larger samples (d >300 µm), and thus for the sake of brevity are not shown here, in a small fraction of the 300-212 µm powders the microstructure has changed drastically. This change is first observed in samples in the 300-212 µm size fraction and the prevalence of such structures has been observed to increase with decreasing sieve fraction and, therefore, with the rise in the cooling rate. **Figure 5** depicts the microstructure of one such 300-212 µm sample, which shows the formation of a region with very fine microstructure where nucleation has most likely been

initiated as dendritic α-Al emerges from this region (this refined structure will be referred to as an angular structure throughout this work as it often displays a straight side morphology with distinct angular points). Beyond this angular region solidification proceeds as in the larger powders: cellular α-Al and dendritic α-Al with interdendritic lamellar eutectic. What is interesting here is that the morphology of the nucleation zone is rather angular (probably cube-like with depressed faces in 3D) instead of circular (spherical in 3D). In most samples displaying such zones, the morphology of these regions was similar (this will be presented later). EDX analysis was performed on these angular regions for all sample sizes. Regardless of the sample size, the composition of the solute in this region was measured as 4 ± 0.1 wt% Fe and 1 ± 0.15 wt% Si. It is worth noting here that while Fe content is the same as the composition of the melt, while the Si content being lower (Al-4.1 wt% Fe-1.9 wt% Si).

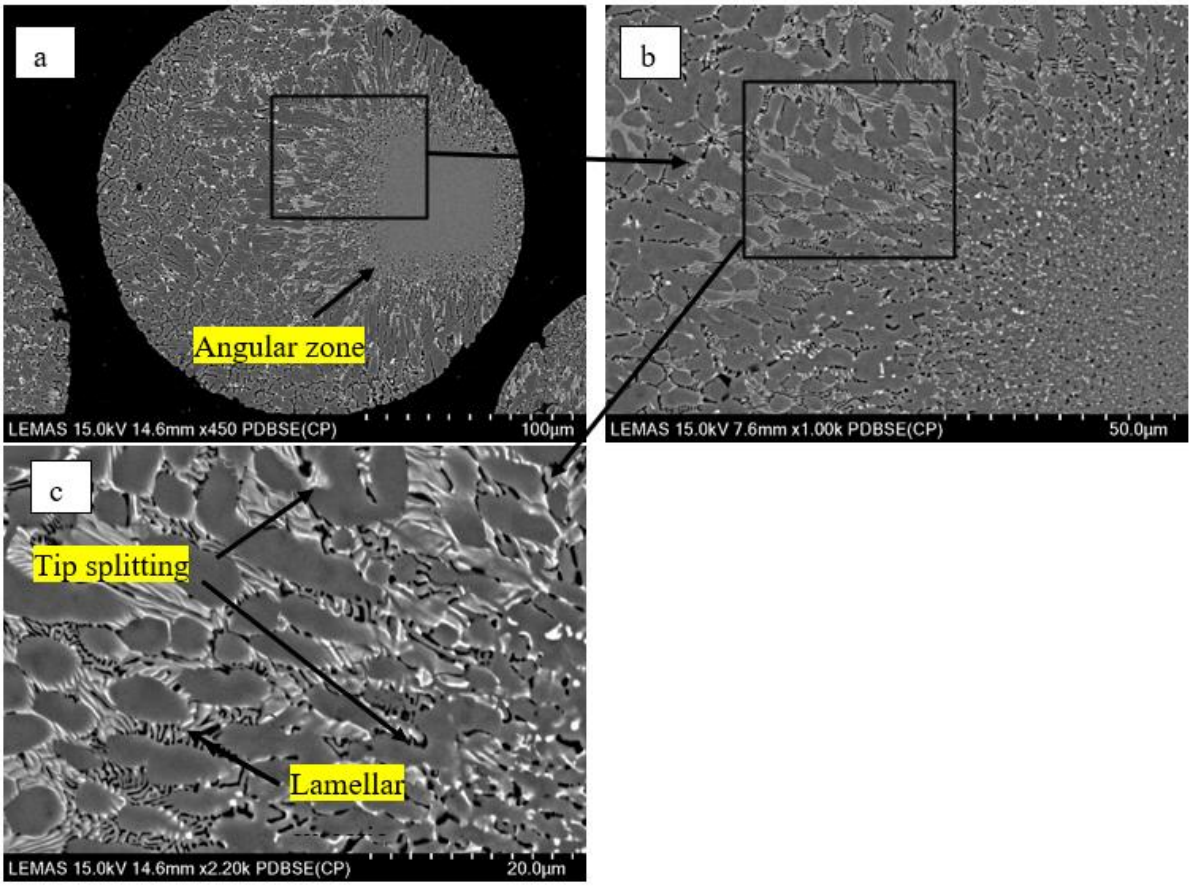

Figure 5: SEM micrographs showing featureless angular nucleation zone and lamellar interdendritic eutectic in a 300-212 µm sample.

As discussed earlier, decreasing the sample size increases the fraction of samples with these angular nucleation zones, this being more obvious in **Figure 6a** which exhibits a low magnification microstructure of a random sample of 150-106 µm powders. Roughly half of the sample display one or more internal angular zone(s). Moreover, some samples, as shown in

Figure 6b and **c,** clearly display multiple angular regions. The morphology of the two angular regions depicted in **Figure 6c** are clearly different from each other: one being (near) square, while the other one is triangular. α-Al dendrites are observed to grow out of the angular zones, with a clearly delineated boundary where the two sets of dendrites meet. **Figure 6d** depicts what appears to be four of the refined zones, each of which adopts a more circular-like morphology as compared to others depicted in **Figure 6b** and **c**. Moreover, the centres of these refined zones delineate the four corners of a square.

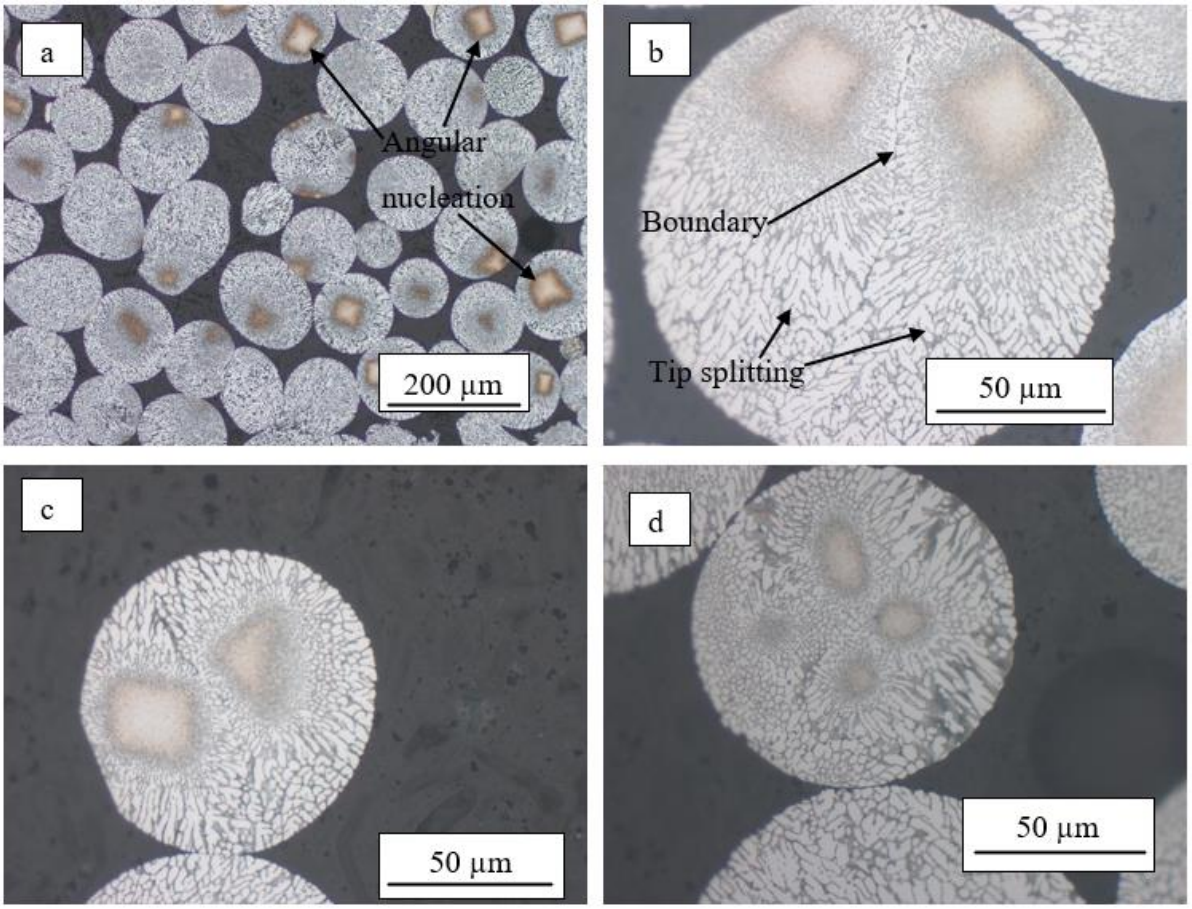

Figure 6: OM microstructures of various 150-106 µm samples a) half of the samples depicting an angular zone, b) and c) showing two nucleation zones in the samples separated by a boundary d) different cross section view of an angular zone.

The SEM micrographs given in **Figure 7** provide a higher magnification view of two 150-106 µm droplets, showing detail of the angular zone. **Figure 7b** shows that the angular zone probably consists of very fine precipitates (confirmed below via TEM), transitioning into normal dendritic growth as moving away from the centre of the angular region to its periphery. Moreover, approaching to the periphery of the angular zone, the precipitates become coarser and hence visible in the SEM. However, For the most part the structure inside the angular region is so fine as to be below the resolution limit of the SEM. Beyond the angular zone

solidification proceeds via a mixed structure of divorced eutectic, cellular α-Al and dendritic α-Al.

Figure 7c exhibit a droplet from the 150-106 µm sieve fraction displaying two nucleation zones: one featureless the other cellular. This difference in microstructure is probably due either to the sectioning angle of the sample or due to the two regions being nucleated at slightly different times and hence at different undercoolings. As shown in **Figure 7b** cellular α-Al forms on the periphery of the angular featureless region while **Figure 7d** reveals the lamellar nature of the interdendritic eutectic.

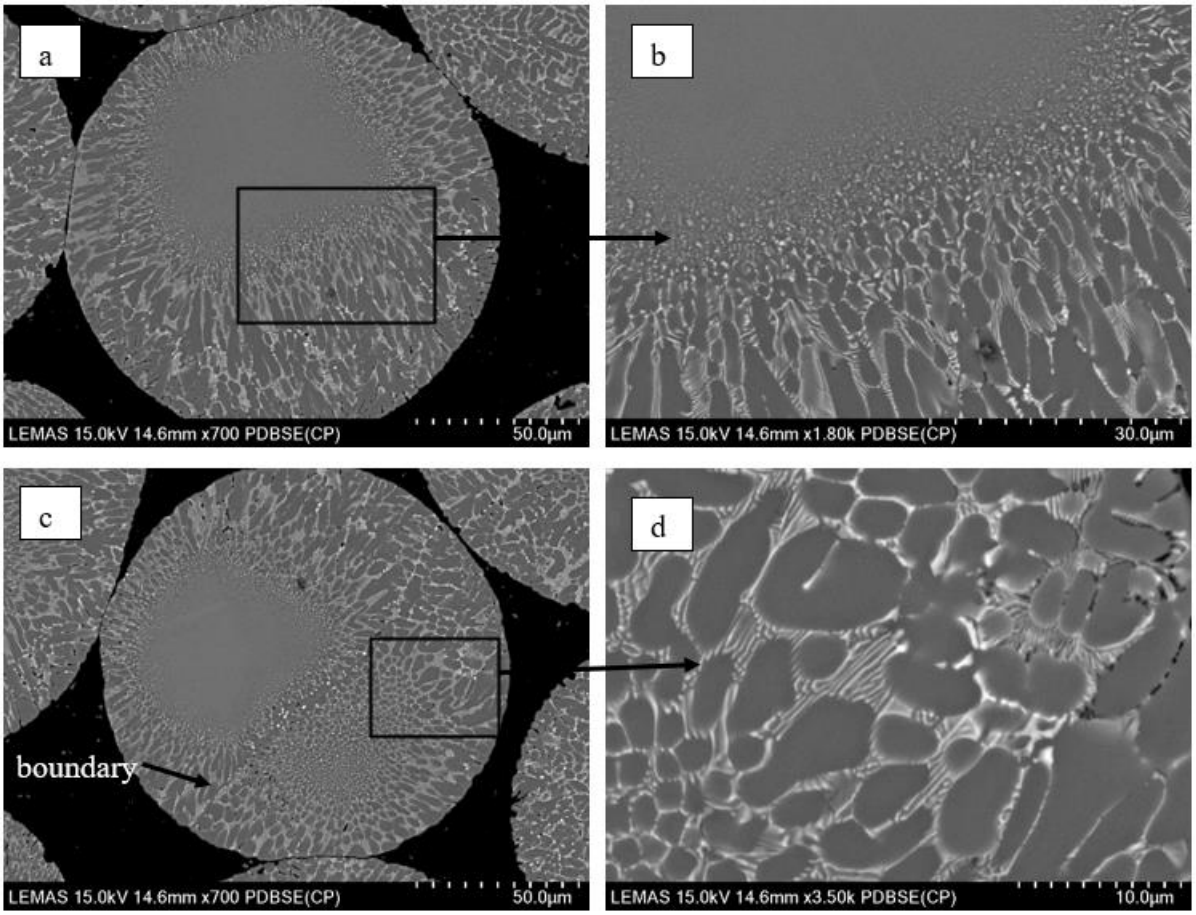

Figure 7: SEM microstructures of 150-106 µm samples with a) a single and c) two angular zone(s) and magnified images of them exhibiting b) the transition zone and d) lamellar eutectic.

Samples with d < 106 µm have a number of different microstructures. In addition to the above-mentioned angular structures, propeller-like structures have also been observed in these samples, albeit these appear to be composed of the same featureless material as the angular regions. **Figure 8** depicts the morphologies of selected structures as identified in the 106-75 µm size fraction. **Figure 8a** shows an early period of the growth of such structure, wherein the arms of the propellers are smaller than the others in the figure. This propeller-like structure has

four arms radiating from a single nucleation point where the angle between neighbouring arms is a right angle. A similar, if somewhat better developed, structure is shown in **Figure 8b**. As seen in **Figure 8b**, one of the arms of the propeller-like structure has grown to the centre of the sample covering nearly the half of the sample. The arm growing towards the centre of the droplet is longer than the other arms. Moreover, the shortest arm is the one which grows to the opposite site of the longest arm, although this may simply reflect the available space for growth due to the proximity of the droplet surface. A fully grown version of propeller-like structure is given in **Figure 8c**. Similar to **Figure 8b**, one arm has grown almost to the other side and nearly reached the circumference of the spherical droplet. The arms of the propeller-like structures given in **Figure 8b** and **c** are thinner at the nucleation point and gets thicker gradually. After reaching a peak, the thickness decreases drastically forming a sharp tip. **Figure 8d** depicts propeller-like structure whose arms growing out of the nucleation point. While the propeller-like structures shown in **Figure 8a** and **b** have four arms growing at right angles, those depicted in **Figure 8c** and **d** have three arms growing from circular central hub, with the angle between the arms being close to 120°.

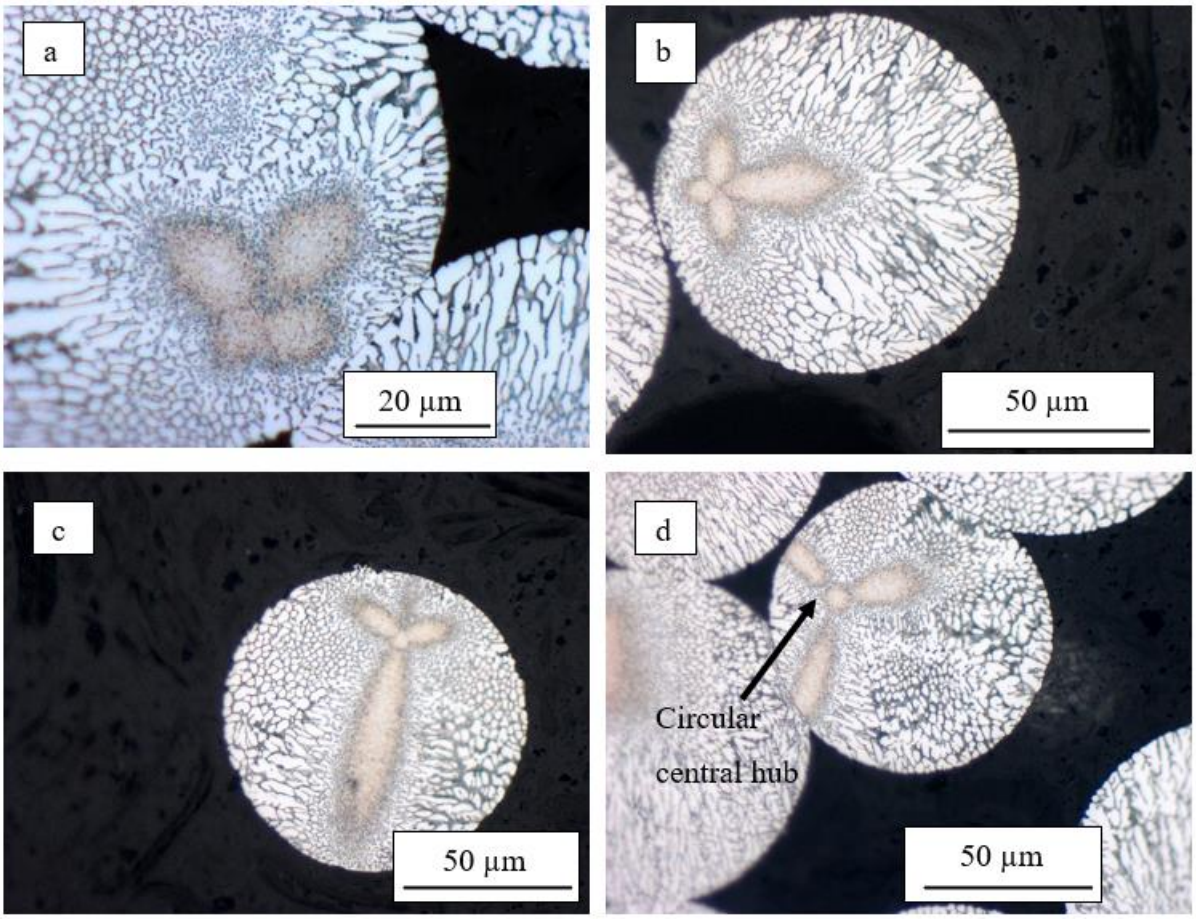

Figure 8: OM microstructures showing propeller-like structures observed in the 106-75 µm

samples at various stage of the growth a) initial stage, b) one arm has outgrown other arms c) one arm has covered almost whole sample and d) 3-armed propeller with a central hub

Apart from propeller-like and the angular structure described above, some powders with d < 106 µm have shown what was referred in our previous work on binary Al-Fe alloys(Abul et al. 2022a; Abul, Cochrane, and Mullis 2022b) as Y-shaped structures. Examples of Y-shaped structures observed in the 75-53 µm sieve fraction are provided in **Figure 9**, including a closed kite-like shape (**Figure 9a**) and a dendrite-like morphology (**Figure 9c**). In our previous work (Abul et al. 2022b), these Y-shaped structures was covered in detail and have been shown to comprise fragmented sheet-like structures which are extended in 2D and short in 1D so that the morphology persists with depth during serial sectioning of the sample. The fragmented nature of these structures is clearly visible in **Figure 9b** and is probably due to re-melting immediately following recalescence. The growth of α-Al dendrites from the individual fragments in **Figure 9b** indicates that the observed fragmentation was complete before the growth of these dendrites. Moreover, α-Al dendrite tip splitting is highly pronounced as labelled in **Figure 9a.**

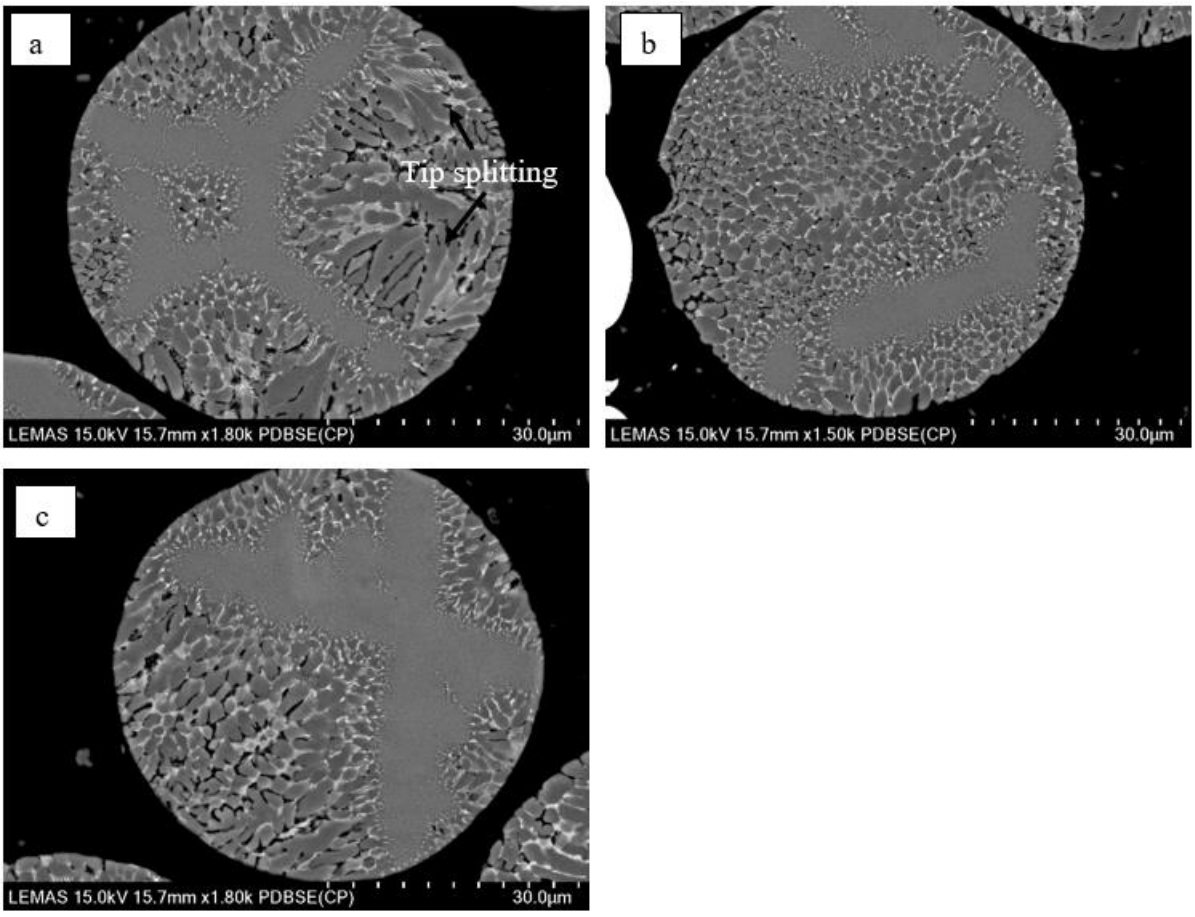

Figure 9: SEM micrographs depicting Y-shaped structures in 75-53 µm samples.

3.3 Eutectic spacing

Figure 10 gives the measured eutectic spacings of drop-tube atomised samples as a function of the cooling rate. It has been found, as expected, that the eutectic spacing is to decrease with increasing cooling rate where it 0.76 µm in the 850-500 µm sieve fraction, with this figure dropping to 0.15 µm in the fastest cooled samples (75-53 µm). However, the 300-212 µm and 212-150 µm size fractions have similar eutectic spacings of around 0.36 µm. In this regard it is worth noting here that the occurrence of the featureless angular zone was initially distinguished in 300-212 µm size fraction at the onset of this plateau. It must also be reminded the reader that the prevalence of the angular zone increases with rising cooling rate.

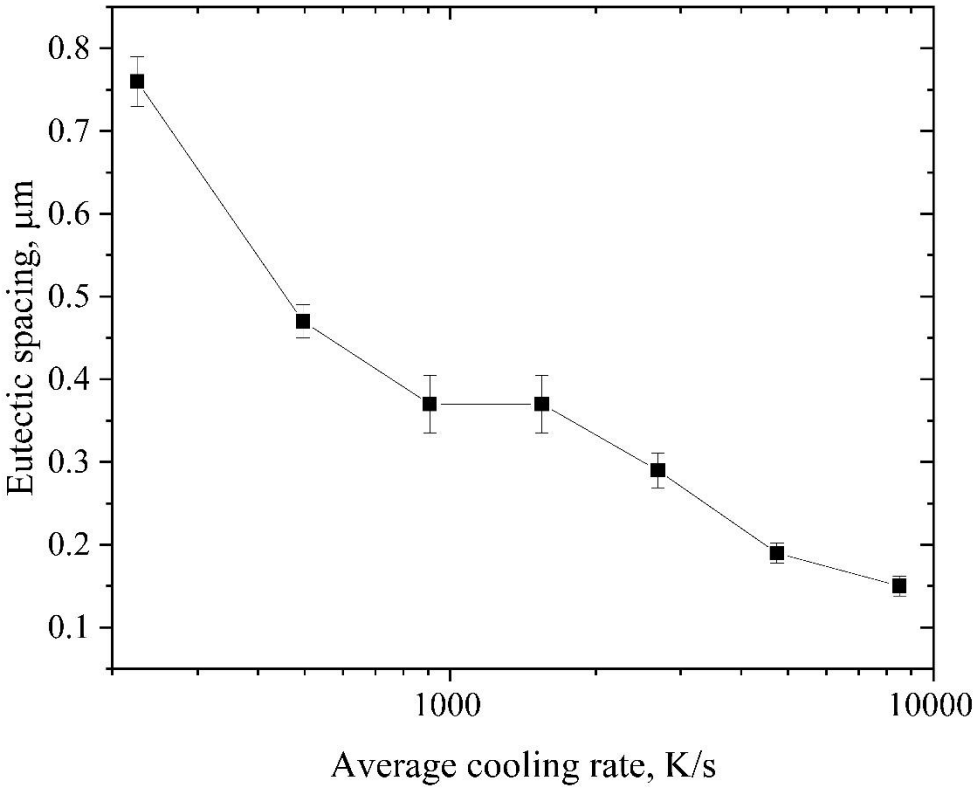

Figure 10: Relation between cooling rate and eutectic spacing

3.4 TEM results

Two FIB sections have been taken for TEM analysis from the angular and the interdendritic regions of a 150-106 µm droplet. TEM results for the angular region are given in **Figure 11** and for the interdendritic region in **Figure 12**. **Figure 11a** shows that there are nano-sized particles with a diameter of less than 100 nm in an α-Al matrix in the angular region. These

particles have clearly defined faceted interfaces, wherein the size and faceting are strongly suggestive of precipitation in the solid-state. Moreover, these precipitates have formed in clusters, with each cluster being the combination of several precipitates but with variable numbers of precipitates within each cluster. **Figure 11b-d** shows the EDX mapping of **Figure 11a**, revealing that these faceted phases are ternary Al-Fe-Si intermetallics. Moreover, quantitative EDX analysis has also been undertaken from these precipitates as well as the matrix. The elemental composition of the matrix contains 0.15 at.% Fe and 0.71 at.% Si, both of which significantly exceed their equilibrium solubilities in α-Al. EDX analysis of the precipitates have been taken from the areas designated as 1 and 2 in **Figure 11a**. The reason behind the selection of these locations for EDX analysis was the presence of relatively large clusters and, therefore, it is high likely to get the true composition of the precipitate material compared to smaller precipitates more accurately, there being less chance of the electron interaction volume overlapping with the surrounding matrix. The chemical composition of region 1 and 2 was analysed to be very similar and is given as 72 at.% Al, 19.5 at.% Fe and 8.5 at% Si, which corresponds the ternary Al_8Fe_2Si intermetallic (Mondolfo n.d.). Moreover, TEM SAD pattern (**Figure 11e**) taken along $(2\bar{3}0)$ zone axis from the region marked as 1 in **Figure 11a** have shown the presence of Al_8Fe_2Si.

Figure 12 shows a TEM micrograph of the interdendritic region of a 150-106 μm sample, which contains lamella type interdendritic eutectic. **Figure 12b-d**, which give the EDX mapping of the view shown in **Figure 12a**, confirms that the intermetallic component of the eutectic is a ternary compound of Al, Fe and Si. The EDX analysis from the regions labelled 1 and 2 in **Figure 12a** has revealed the composition of the intermetallic as 72 at.% Al, 19 at.% Fe and 9 at.% Si, which is very similar to the composition of the intermetallic precipitates (**Figure 11a**). SAD pattern (**Figure 12e**) taken along $(2\bar{3}0)$ zone axis from the region labelled as 1 in **Figure 12a** have shown that this phase is Al_8Fe_2Si. In other words, both the intermetallics in the eutectic (**Figure 12a**) and in the angular (**Figure 11a**) regions have the same composition, this being within the homogeneity range for Al_8Fe_2Si.

As it was not possible to undertake EDX in the SEM on the rod-like eutectic within the master alloy, further TEM analysis has been undertaken in order to confirm that the intermetallic phase within the rod-like shown in **Figure 3d** is also Al_8Fe_2Si. The TEM results are given in **Figure 13**. The SAD pattern for this phase is given in **Figure 13e** has revealed that the rod-like phase is Al_8Fe_2Si. Moreover, EDX results from the rod-like intermetallic show the ternary Al_8Fe_2Si

phase, thereby confirming that all samples appear to be composed of just two phases, α-Al and Al_8Fe_2Si, irrespective of the cooling rate imposed upon the sample.

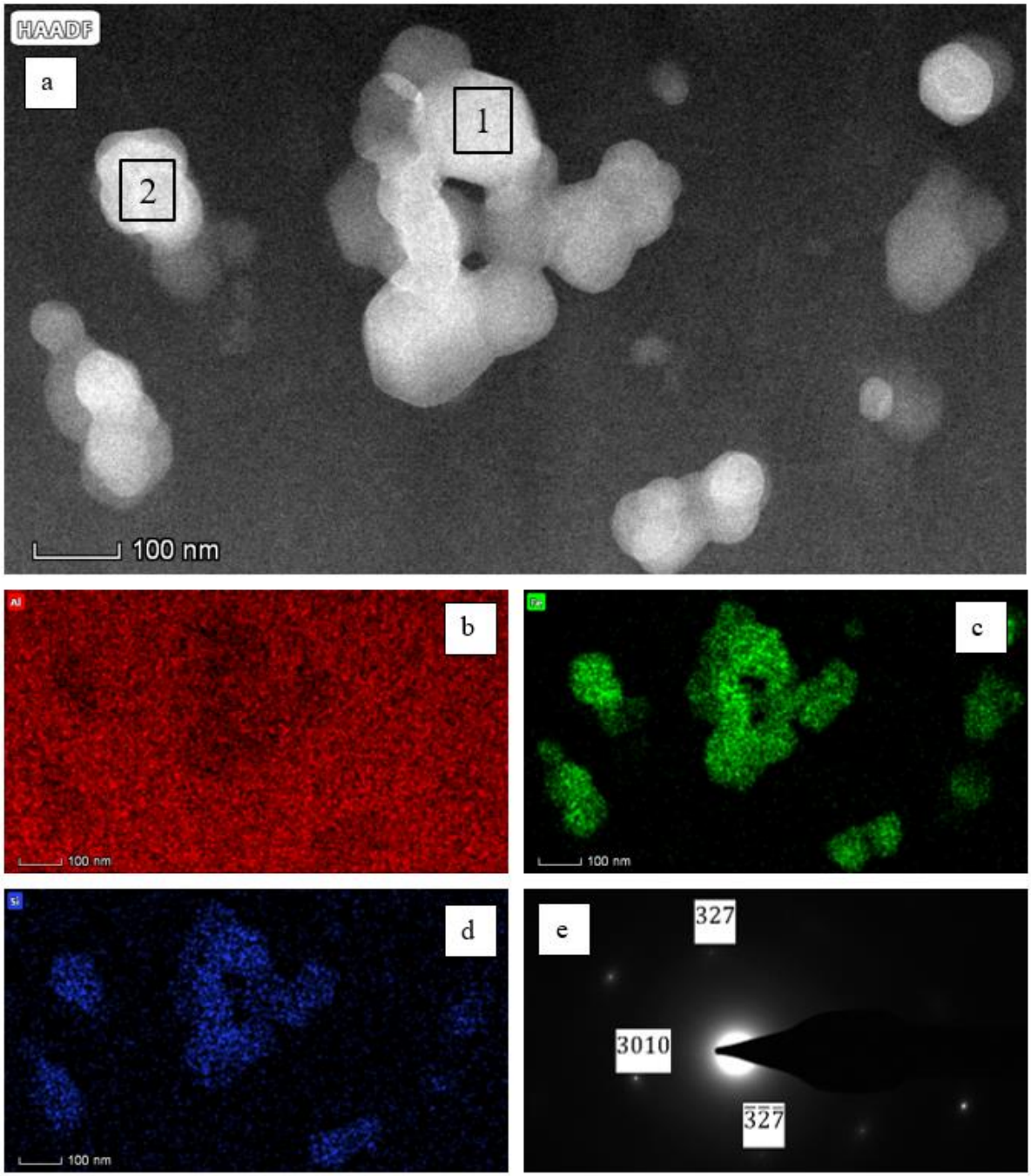

Figure 11: a) TEM image of the angular region taken from a 150-106 µm sample and corresponding EDS maps of b) Al, c) Fe and d) Si, and e) SAD pattern from $(2\bar{3}0)$ zone axis of Al_8Fe_2Si from the region 1 as labelled in a)

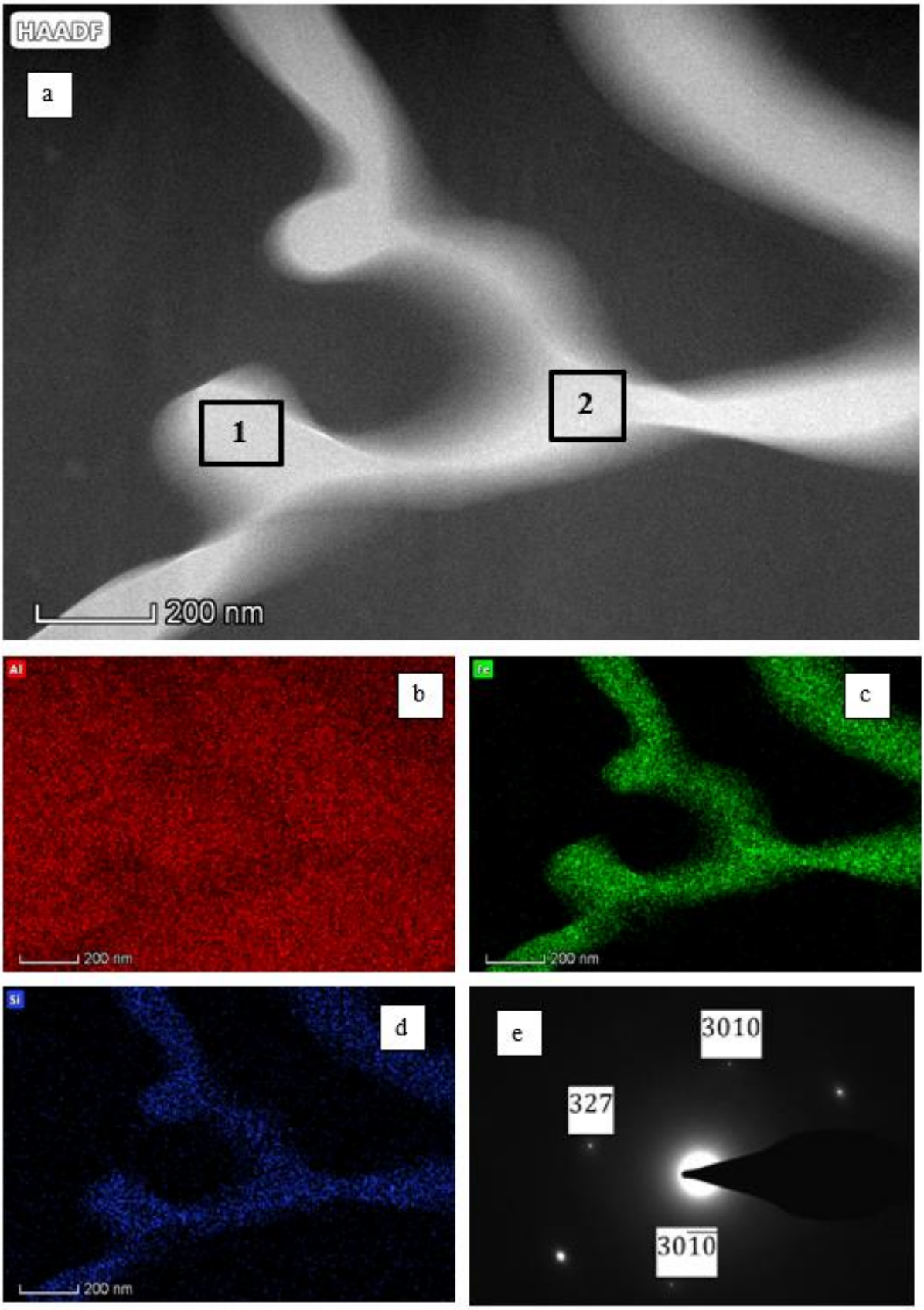

Figure 12: a) TEM micrograph of lamellar eutectic and corresponding EDS maps of b) Al, c) Fe and d) Si, and e) SAD from region 1 showing ternary Al_8Fe_2Si phase from $(2\bar{3}0)$ zone axis.

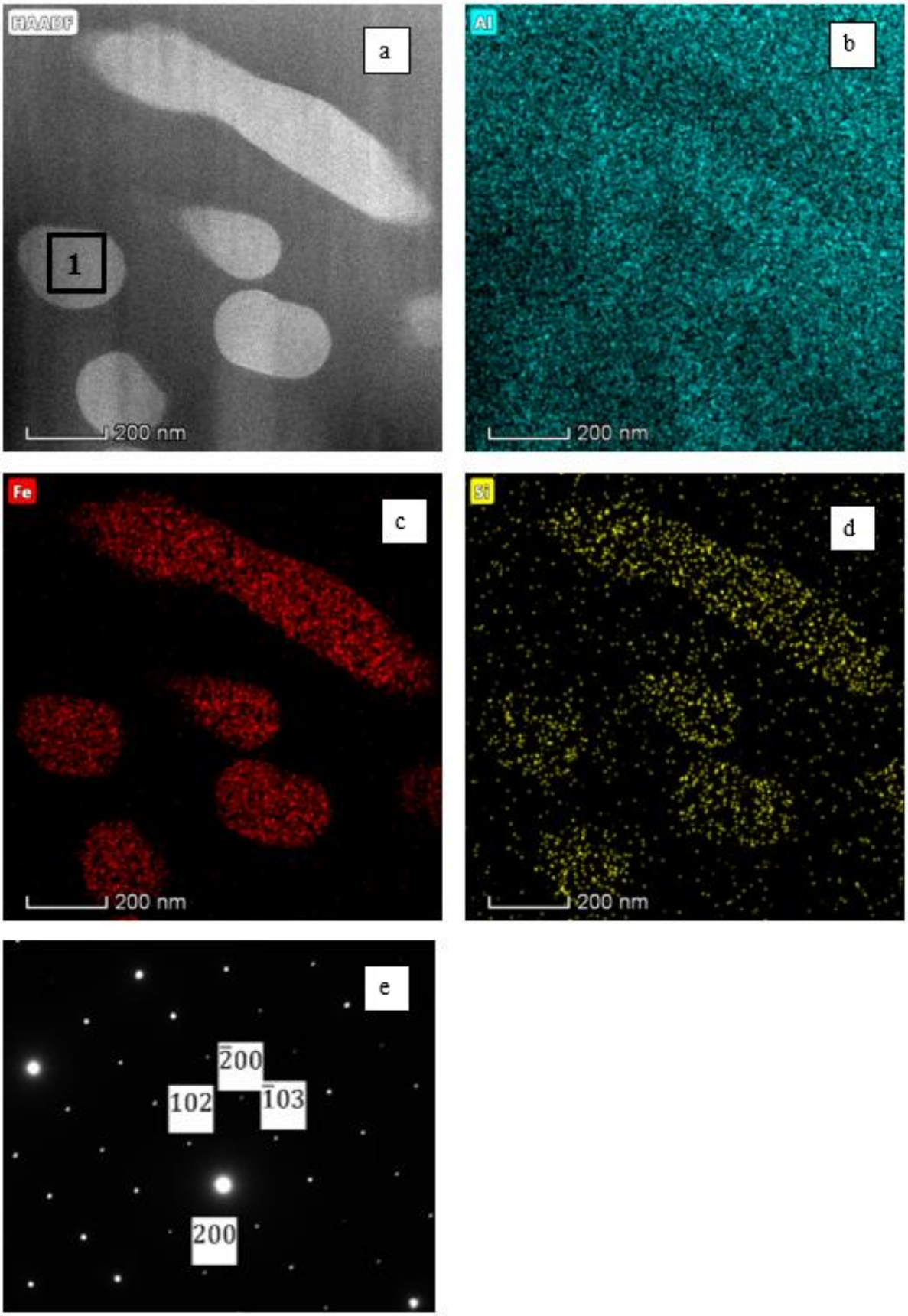

Figure 13: a) TEM image of the rod-like intermetallic, EDS maps of b) Al, c) Fe and d) Si and e) SAD pattern taken from the region 1 as marked in a) showing the ternary Al_8Fe_2Si phase from (010) zone axis.

3.5 Mechanical Properties

3.5.1 Microhardness

Figure 14 shows the effect of the cooling rate on the microhardness of the drop tube atomised samples. The largest sieve fraction (850-500 µm) shows the minimum measured microhardness of 72 ± 2 $HV_{0.01}$. This number has improved with decreasing sample size reaching the highest of 90 ± 3 $HV_{0.01}$ in the 212-150 µm sample, which indicates 30% rise in the microhardness. However, the microhardness slightly decreased as the cooling rate was further rose. That is, the figure for the fastest cooled sample (75-53 µm) was found to be 10% less than the peak value, being 80.2 ± 2.4 $HV_{0.01}$. It is worth noting here that the angular structures first appear in the 300-212 µm samples and 50% of the 212-150 µm samples have formed such structures. Moreover, the majority of droplets with d < 150 show angular structures with fine faceted precipitates.

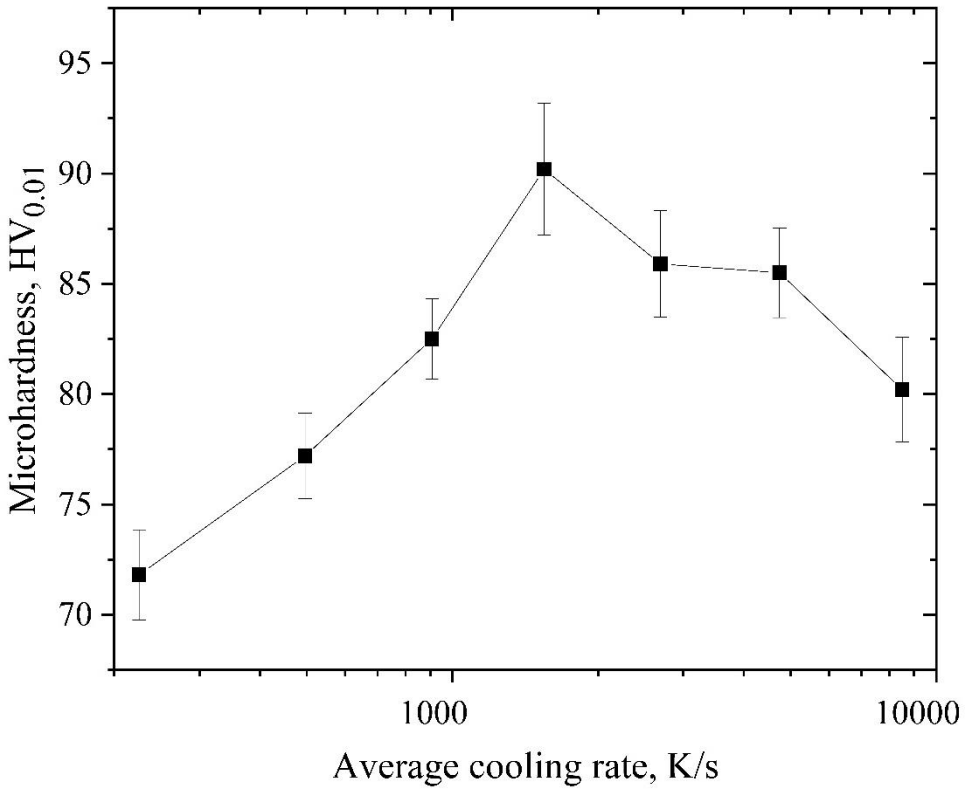

Figure 14: Microhardness (in $HV_{0.01}$) of samples with varying cooling rates.

3.5.2 Nanohardness

In order to understand the mechanical properties of the angular region, nanohardness tests were applied on two 75-53 μm samples. The results are given in **Figure 15** and **Table 1**. The maximum load chosen for the sample given in **Figure 15a** is 15 mN while for the sample in **Figure 15b** is 20 mN. Three measurements namely 2, 3 and 6 as labelled in **Figure 15a** and **b** were taken from the angular region. The nanohardness for this region ranges between 1.69 and 1.86 GPa, the average being 1.76 $\pm$ 0.04 GPa. This figure is around 35% higher than the average nanohardness of the dendritic region (4 and 5) which has an average of 1.3 $\pm$ 0.09 GPa. Moreover, the elastic modulus for these regions have also been measured and are given in **Table 1**. The elastic moduli for angular region and dendritic region were found to be very close at 74 GPa and 67.6 GPa, respectively.

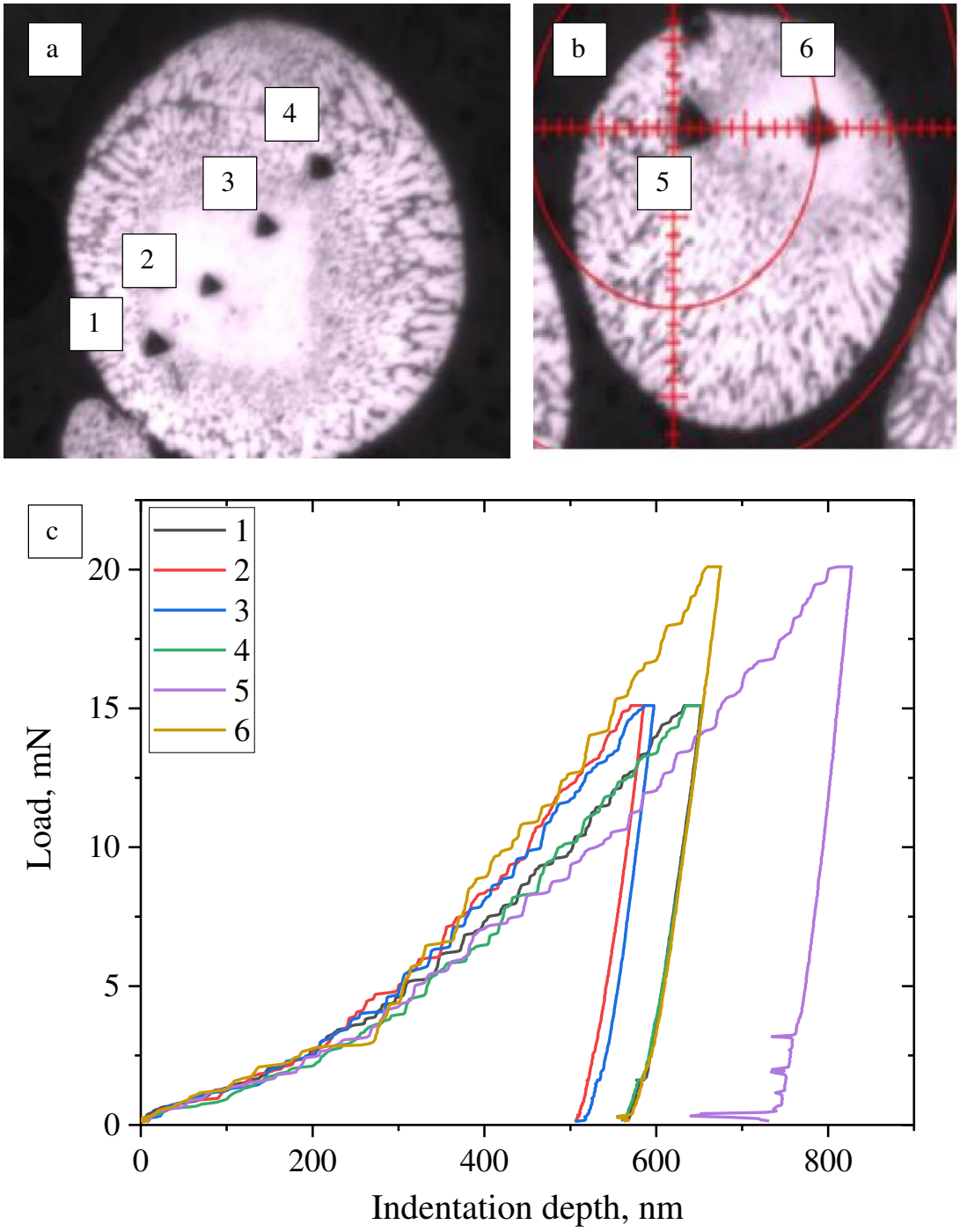

Figure 15: Nanohardness results showing a) and b) the microstructure from where the nanohardness measurements were taken and c) load as a function of penetration depth.

Table 1: Nanohardness and elastic modulus of the angular region, dendritic/eutectic region and the boundary between these two regions. The locations for the measurements are given in **Figure 15a** and **b**.

Indent number	Nanohardness, GPa	Elastic Modulus, GPa
1	1.44	63.25
2	1.74	81.22
3	1.69	76.33
4	1.43	65.51
5	1.18	69.64
6	1.86	64.50

4. Discussion

Al-4.1 wt% Fe-1.9 wt% Si master alloy was atomized using a 6.5 m drop-tube, with powders between 850 μm and 53 μm being produced. Although various microstructures have been observed, XRD results, as provided in **Figure 2** have, somewhat surprisingly, revealed that there are only two phases in all samples, namely α-Al and the ternary intermetallic Al_8Fe_2Si. The Al_8Fe_2Si intermetallic is observed to display various morphologies including; large scrip-like proeutectic particles, rod-like and lamellar eutectic and faceted nano-sized precipitates. TEM analysis, including both SAD and EDX determination (**Figures 11-13**) confirm that in all instance the intermetallic phase is Al_8Fe_2Si. That is, with increasing cooling rate a microstructure comprising irregular script-like proeutectic Al_8Fe_2Si and a rod-like eutectic between α-Al and Al_8Fe_2Si is transformed into a structure consisting of α-Al dendrites and an α + Al_8Fe_2Si lamellar interdendritic eutectic. Similar findings have been reported by (Khalifa et al. 2003; Zhang et al. 2009) which have shown that Al_8Fe_2Si transitions from an irregular structure to a regular lamellar-like morphology as the cooling rate increases. It is unusual that the same two phases should form both a rod-like and a lamellar eutectic under different growth conditions. It can be supposed here that the interdendritic liquid contains much higher concentrations of Fe and/or Si than that of the residual liquid in the master alloy following proeutectic growth of Al_8Fe_2Si, with a higher volume fraction of Al_8Fe_2Si in the eutectic resulting in a change from the rod-like to the lamellar morphology.

Regardless of the experienced cooling rate, α-Al dendrite tip splitting has occurred in all atomized samples. However, this was not observed in our previous studies on drop-tube atomized Al-2.85 wt% Fe and Al-3.9 wt% Fe alloys(Abul et al. 2022a, 2022b). Dendrite tip

splitting is because of the departure from the local thermodynamic equilibrium which, at high growth rates, causes a kinetic instability in the α-Al dendrite tips. It thus appears as if the addition of Si has produced an instability, giving rise to the dendrite tip splitting. This may be due to the somewhat steeper liquidus slope for Al-Si relative to Al-Fe, giving rise to a higher solutal undercooling making any instability more pronounced.

In large drop-tube atomized samples (d > 300 μm) the microstructure consists of a microcellular region which later grows into a dendritic zone. However, with increasing cooling rate a featureless angular zone begins to emerge, with this first being evident in the 300-212 μm size fraction. EDX results from these angular regions reveal that the Fe content is same as the melt, while the Si content was lower than the melt regardless of the cooling rate. That is, within these angular regions, solidification appears to be partitionless as for Fe, but not as for Si. For both Fe and Si in Al, relatively low undercooling is required to access the T_0 temperature and it can be conjectured that the difference may be due to differences in the diffusivities of Fe and Si in liquid Al. The diffusivity of Fe in liquid Al has been reported to be anomalously low because Al atoms form clusters around Fe atoms in the melt (Isono et al. 1996). According to (Du et al. 2003) the diffusivities of Si, D_{Si}^{L}, and Fe, D_{Fe}^{L}, in liquid Al at 900 K are estimated as 2.4 x 10^{-9} m^2 s^{-1} and 2.17 x 10^{-10} m^2 s^{-1}, respectively.

TEM results (**Figure 11**) have revealed that the angular zone, where the solidification in the droplet was initiated, comprises clusters of nano-sized (with a diameter of ~ 100 nm) faceted ternary Al_8Fe_2Si intermetallic in the matrix. Both the size of the ternary particles and their faceted nature suggest this phase has evolved because of solid-state decomposition rather than from the liquid. Given, as discussed above, that the bulk Fe composition of the angular region is the same as the melt, it can be conjecture that conjecture that solidification which was partitionless with respect to Fe has resulted in α-Al that is highly supersaturated in Fe and which is thus highly metastable, with solid-state decomposition to a less supersaturated solid-solution and faceted Al_8Fe_2Si precipitates occurring soon after formation, while the droplet was still at elevated temperatures. It must be noted here that these faceted intermetallics have formed clusters. This is probably due to the first such precipitate acting as a heterogeneous nucleation site for other precipitates, thus resulting in cluster formation. This would occur if the nucleation barrier were more of an obstacle to growth than diffusion of either Fe or Si, i.e., it is indicative of nucleation limited growth.

In many cases the angular morphologies appear approximately square but with concave sides, with the proposed 3D morphology being shown schematically in **Figure 16**. Such a morphology would be a natural consequence of the growth of a faceted morphology as the growth of the faces of the cubes is slowed down due to solute accumulation (note that Si is the only solute because of the partitionless growth as for Fe). Consequently, the edges of the cube grow faster than the faces, resulting in the somewhat concave faces observed. Similar structures have been observed directly in Cu_9Al_4 crystal extracted by deep etching (Xian et al. 2015) and would explain the morphology observed in **Figure 6d**, in which the featureless material forms in four regions tracing the outline of a square. This morphology would arise if the structure shown in **Figure 16** were sectioned such that the corners of the cube were visible but the edges and face were not because they were below the level of the sectioning plane. Moreover, an order of magnitude estimate of the diffusion length scale appears consistent with the formation of such concave sides cubes.

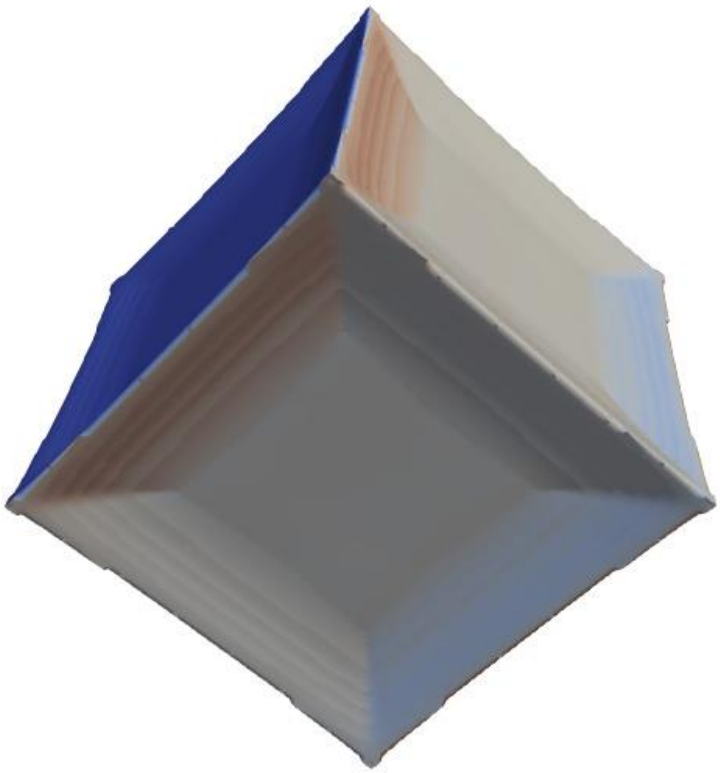

Figure 16: 3D simplified illustration of the angular region depicting depressed faces.

The characteristic diffusion length, $\bar{x}$, is given by

$$\bar{x} = \sqrt{2Dt} \tag{2}$$

where t and D are the time available for solidification and the diffusion coefficient, respectively. The solidification time, t, for a 150 µm sample is calculated as 0.018 s, based upon a cooling rate of R = 1870 K s^{-1} with the latent heat and specific heat for liquid Al being L = 396 kJ $kg^{-1}$and c_p = 1180 J kg^{-1} K^{-1} (Chu and Granger 1990) respectively. The diffusion coefficient for Si at 930 K (the melt was assumed to be undercooled by 90 K prior to solidification) was estimated as 1.34 x 10^{-9} m^2 s^{-1} (Du et al. 2003). Substituting these in **Equation 2** gives $\bar{x}$ = 31.5 µm. This figure is close to the size of the angular region given in **Figure 6** and **7**. Thus, the solute (Si) build up in at the faces angular region would be consistent with the formation of depressions of the cube's face.

In addition to the angular structures described above, both Y-shaped (**Figure 9**) and propeller-like structures (**Figure 8**) have also been analysed in small (d < 106 µm) samples. The Y-shaped structures have been extensively discussed in our previous work(Abul et al. 2022b) on drop-tube atomized binary Al-3.9 wt% Fe alloy. It was found that the Y-shaped features are composed of internally connected sheet-like morphologies also resulting from an initially partitionless solidification resulting in α-Al that is highly supersaturated in Fe subsequently undergoes a solid-state decomposition to both needle-like and nano-sized spherical precipitates. Thus, no attempt has been made here to further analyse the Y-shaped morphology. Propeller-like structure formed in the samples have either three or four arms. They are likely a natural evolution of the cube-like structure with depressed faces, described above. As the undercooling together with cooling rate increases with decreasing sample size, the growth characteristic will change from faceted (angular zone) to continuous. The corners of the cube are already outgrowing the edges and faces and a transition to the growth of a {111} dendrite would explain both types of propeller morphology, such {111} dendrites being the morphology observed when faceted growth breaks down in these concave cubes(Xian et al. 2015). While normal {100} cubic growth gives six primary dendrite arms, {111} growth results in dendrites with eight primary arms. Slicing orthogonal to <100> would render four arms with right angles between arms, while slicing orthogonal to <111> would result in three arms with 120° between the arms, the fourth arm being seen head-on and thus appearing as the central hub.

The angular regions appear to be significantly harder than the surrounding dendritic matrix and this is likely due to strengthening both from the supersaturated solid solution and from the nano-scale dispersion of precipitates. What is perhaps more surprising is that after reaching a peak for the 212-150 µm droplet size, the microhardness of the powders should then decrease with decreasing droplet size. This might be because of weak bonding between the angular

region and the surrounding dendritic matrix (see **Table 1**, in which indent 1 on the boundary between an angular region and the matrix has a lower hardness than either the matrix or the angular region). The transition to the propeller-like morphology would then accelerate this decrease in hardness as the interfacial area between the two phases would increase relative to the amount of the harder, featureless phase.

5. Acknowledgements

The authors gratefully acknowledge LEMAS for their support & assistance in this work. The authors also acknowledge Dr Chun Wang for her help in nanohardness.

Corresponding author would like to thank the Republic of Turkey Ministry of National Education, Directorate General for Higher and Overseas Education for their support.

6. References

Abul, Mehmet R., Robert F. Cochrane, and Andrew M. Mullis. 2022a. "Microstructural Development and Mechanical Properties of Drop Tube Atomized Al-2.85 Wt% Fe." *Journal of Materials Science & Technology* 104:41–51.

Abul, Mehmet R., Robert F. Cochrane, and Andrew M. Mullis. 2022b. "Partitionless Solidification and Anomalous Triradiate Crystal Formation in Drop-Tube Processed Al-3.9wt%Fe Alloys." *Materials Today Communications* 103274.

Ahmed, Emad M., and M. R. Ebrahim. 2014. "Microstructure and Microhardness Evolutions of High Fe Containing Near-Eutectic Al-Si Rapidly Solidified Alloy." *Journal of Metallurgy* 2014:1–8.

Chen, J., R. Lengsdorf, H. Henein, D. M. Herlach, U. Dahlborg, and M. Calvo-Dahlborg. 2013. "Microstructure Evolution in Undercooled Al–8 Wt% Fe Melts: Comparison between Terrestrial and Parabolic Flight Conditions." *Journal of Alloys and Compounds* 556:243–51.

Chu, M. G., and D. A. Granger. 1990. "Solidification and Microstructure Analysis of Rapidly Solidified Melt-Spun Al-Fe Alloys." *Metallurgical Transactions A* 21(1):205–12.

Du, Yong, Y. A. Chang, Baiyun Huang, Weiping Gong, Zhanpeng Jin, Honghui Xu, Zhaohui Yuan, Yong Liu, Yuehui He, and F. Y. Xie. 2003. "Diffusion Coefficients of Some Solutes in Fcc and Liquid Al: Critical Evaluation and Correlation." *Materials Science and Engineering: A* 363(1–2):140–51.

Du, Yong, Julius Clemens Schuster, Zi-Kui Liu, Rongxiang Hu, Philip Nash, Weihua Sun, Weiwei Zhang, Jiong Wang, Lijun Zhang, and Chengying Tang. 2008. "A Thermodynamic Description of the Al–Fe–Si System over the Whole Composition and Temperature Ranges via a Hybrid Approach of CALPHAD and Key Experiments." *Intermetallics* 16(4):554–70.

Griger, A., and V. Stefaniay. 1996. "Equilibrium and Non-Equilibrium Intermetallic Phases in Al-Fe and Al-Fe-Si Alloys." *Journal of Materials Science* 31(24):6645–52.

Hu, Ke, Fuxiao Yu, and Qichi Le. 2020. “Investigation on Al 6 Fe Fibers of Al-3 Wt Pct Fe Alloy at Different Mold Temperatures.” *Metallurgical and Materials Transactions B* 51(2):697–708.

Isono, N., Patrick Michael Smith, David Turnbull, and M. J. Aziz. 1996. “Anomalous Diffusion of Fe in Liquid AI Measured by the Pulsed Laser Technique.” *Metallurgical and Materials Transactions A* 27(3):725–30.

Khalifa, W., F. H. Samuel, and J. E. Gruzleski. 2003. “Iron Intermetallic Phases in the Al Corner of the Al-Si-Fe System.” *Metallurgical and Materials Transactions A* 34(13):807–25.

Kiliçaslan, M. Fatih, Fikret Yilmaz, Semra Ergen, Soon-Jik Hong, and Orhan Uzun. 2013. “Microstructure and Microhardness of Melt-Spun Al–25Si–5Fe–XCo (X= 0, 1, 3, 5) Alloys.” *Materials Characterization* 77:15–22.

Li, Shu, Ping Wu, Hiroki Fukuda, and Teiichi Ando. 2009. “Simulation of the Solidification of Gas-Atomized Sn-5mass%Pb Droplets.” *Materials Science and Engineering A* 499(1–2):396–403.

Mondolfo, L. F. n.d. “Aluminium Alloys: Structure and Properties, Butterworths, London 1976.”

Mullis, A. M., T. D. Bigg, and N. J. Adkins. 2015. “A Microstructural Investigation of Gas Atomized Raney Type Al-27.5 at.% Ni Catalyst Precursor Alloys.” *Journal of Alloys and Compounds* 648:139–48.

Simensen, C. J., & Vellasamy, R. 1977. “Determination of Phases Present in Cast Material of an Al-0.5 Wt.% Fe-0.2 Wt.% Si Alloy.” *International Journal of Materials Research* 68(6):428–31.

Ünlü, N., A. Genc, M. L. Öveçoğlu, N. Eruslu, and F. H. Froes. 2001. “Characterization Investigations of Melt-Spun Ternary Al–XSi–3.3 Fe (X= 10, 20 Wt.%) Alloys.” *Journal of Alloys and Compounds* 322(1–2):249–56.

Xian, J. W., S. A. Belyakov, T. B. Britton, and C. M. Gourlay. 2015. “Heterogeneous Nucleation of Cu6Sn5 in Sn–Cu–Al Solders.” *Journal of Alloys and Compounds* 619:345–55.

Young, R. M. K., and T. W. Clyne. 1981. “An AlmFe Intermetallic Phase Formed during Controlled Solidification.” *Scripta Metallurgica* 15(11):1211–16.

Zhang, Lifeng, Jianwei Gao, Lucas Nana Wiredu Damoah, and David G. Robertson. 2012. “Removal of Iron from Aluminum: A Review.” *Mineral Processing and Extractive Metallurgy Review* 33(2):99–157.

Zhang, Yanhua, Yongchang Liu, Yajing Han, Chen Wei, and Zhiming Gao. 2009. “The Role of Cooling Rate in the Microstructure of Al–Fe–Si Alloy with High Fe and Si Contents.” *Journal of Alloys and Compounds* 473(1–2):442–45.

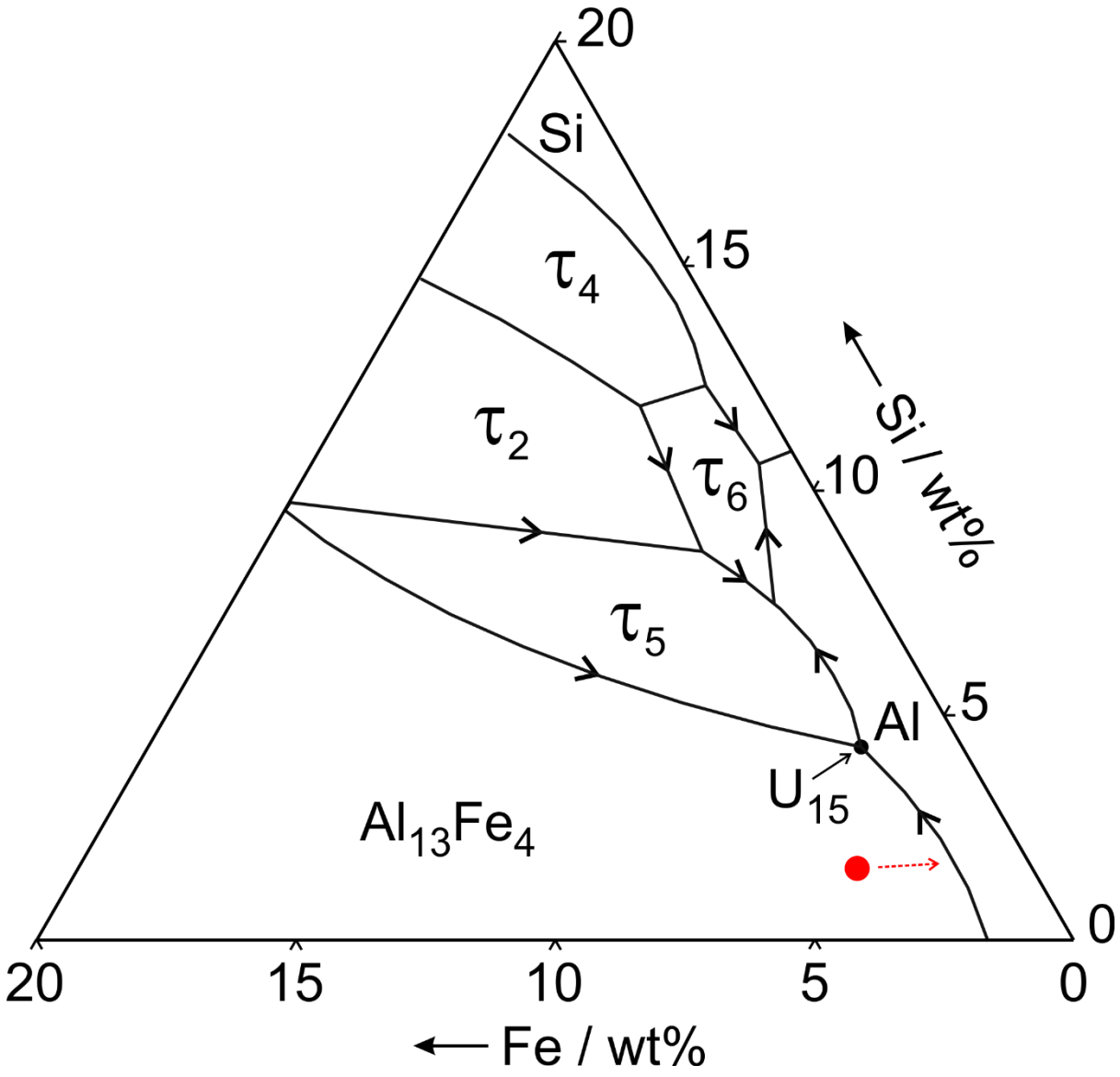
20
Si
15
τ4
τ2
τ6
10
Si / wt%
τ5
5
Al
U15
Al13Fe4
0
20
15
10
5
0
Fe / wt%

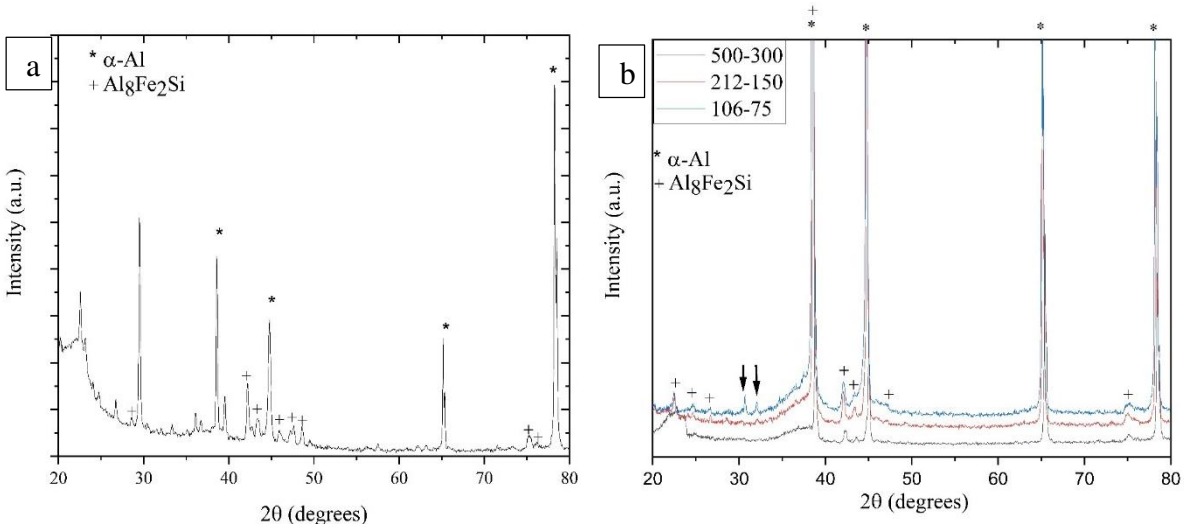
a
* α-Al
+ Al8Fe2Si
Intensity (a.u.)
2θ (degrees)
b
500-300
212-150
106-75
* α-Al
+ Al8Fe2Si
Intensity (a.u.)
2θ (degrees)

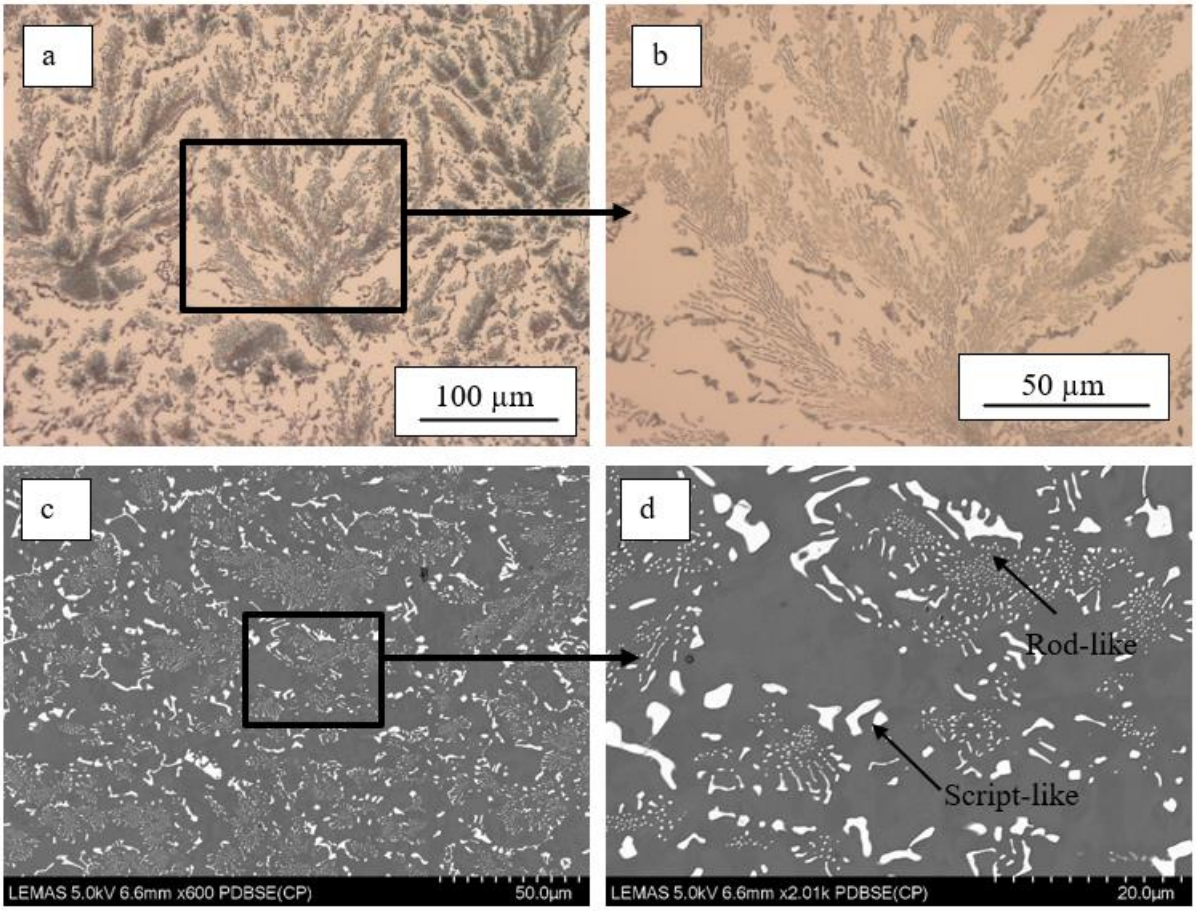
a
100 µm
b
50 µm
c
LEMAS 5.0kV 6.6mm x600 PDBSE(CP)
50.0µm
d
Rod-like
Script-like
LEMAS 5.0kV 6.6mm x2.01k PDBSE(CP)
20.0µm

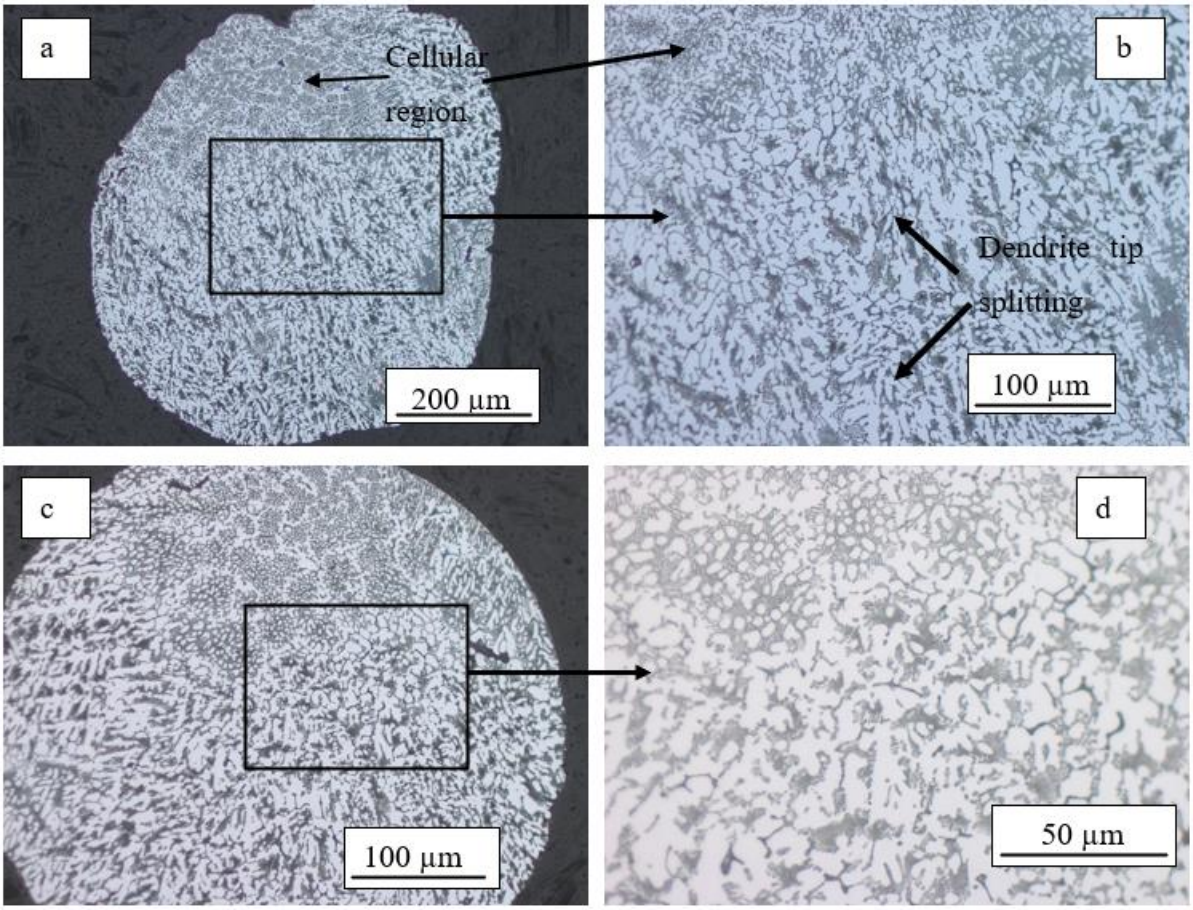
a
Cellular
region
200 µm
b
Dendrite tip
splitting
100 µm
c
100 µm
d
50 µm

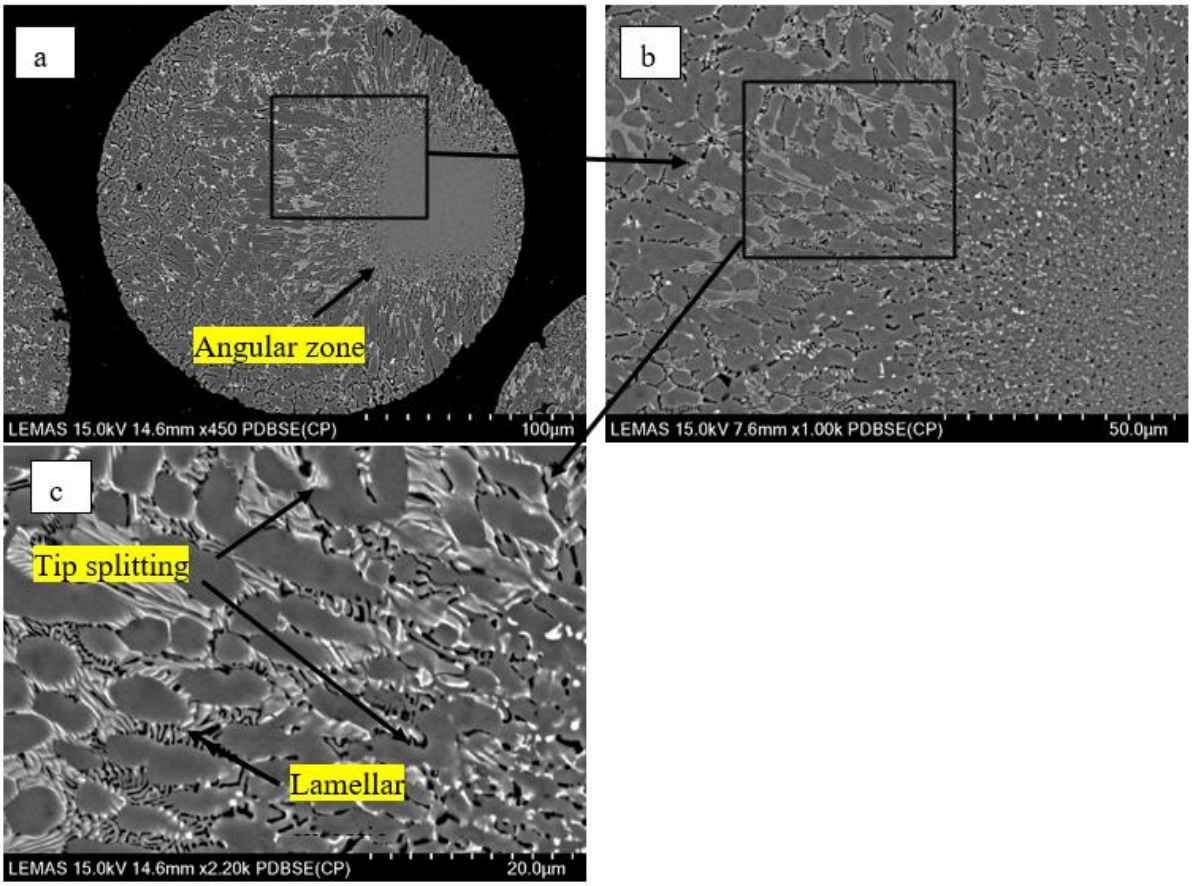
a
Angular zone
LEMAS 15.0kV 14.6mm x450 PDBSE(CP)
100µm
b
LEMAS 15.0kV 7.6mm x1.00k PDBSE(CP)
50.0µm
c
Tip splitting
Lamellar
LEMAS 15.0kV 14.6mm x2.20k PDBSE(CP)
20.0µm

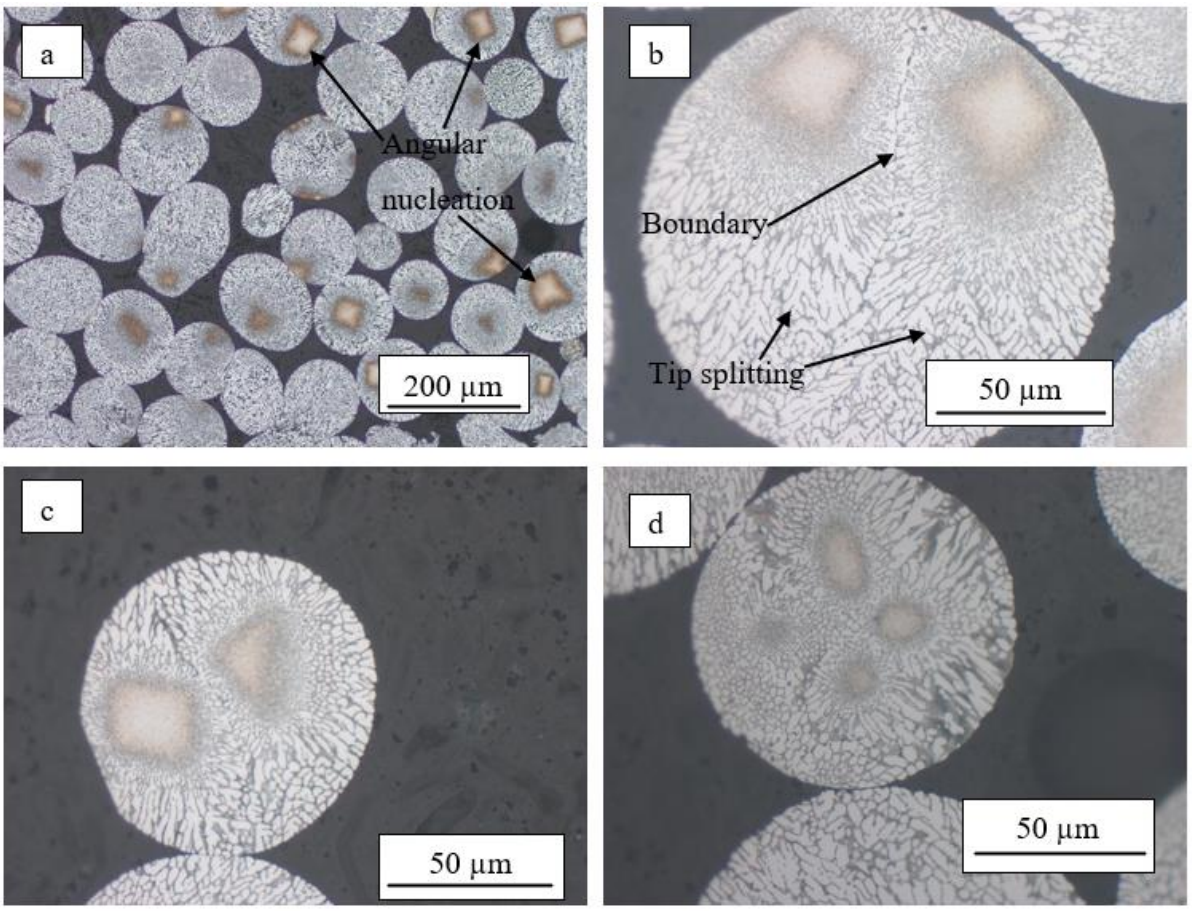
a
Angular
nucleation
200 µm
b
Boundary
Tip splitting
50 µm
c
50 µm
d
50 µm

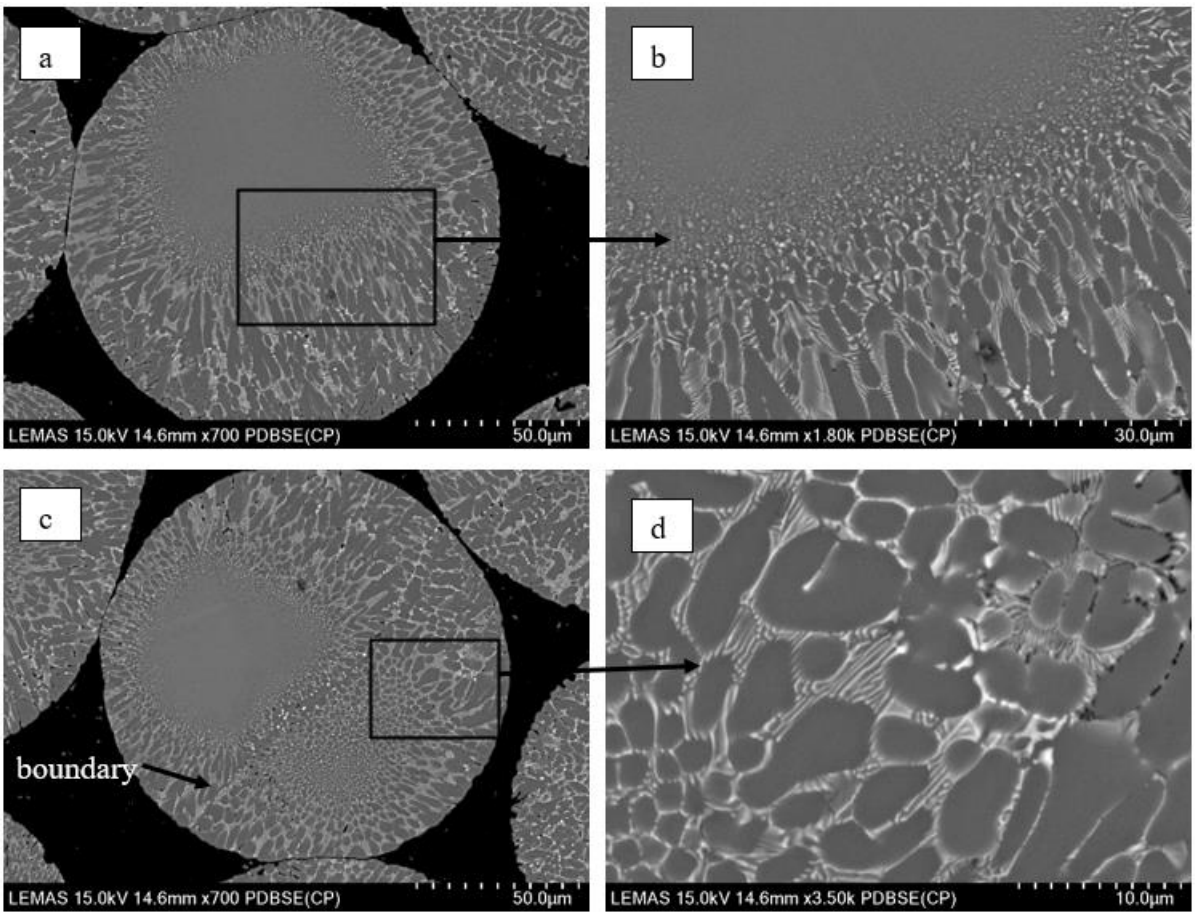
a
LEMAS 15.0kV 14.6mm x700 PDBSE(CP)
50.0µm
b
LEMAS 15.0kV 14.6mm x1.80k PDBSE(CP)
30.0µm
c
boundary
LEMAS 15.0kV 14.6mm x700 PDBSE(CP)
50.0µm
d
LEMAS 15.0kV 14.6mm x3.50k PDBSE(CP)
10.0µm

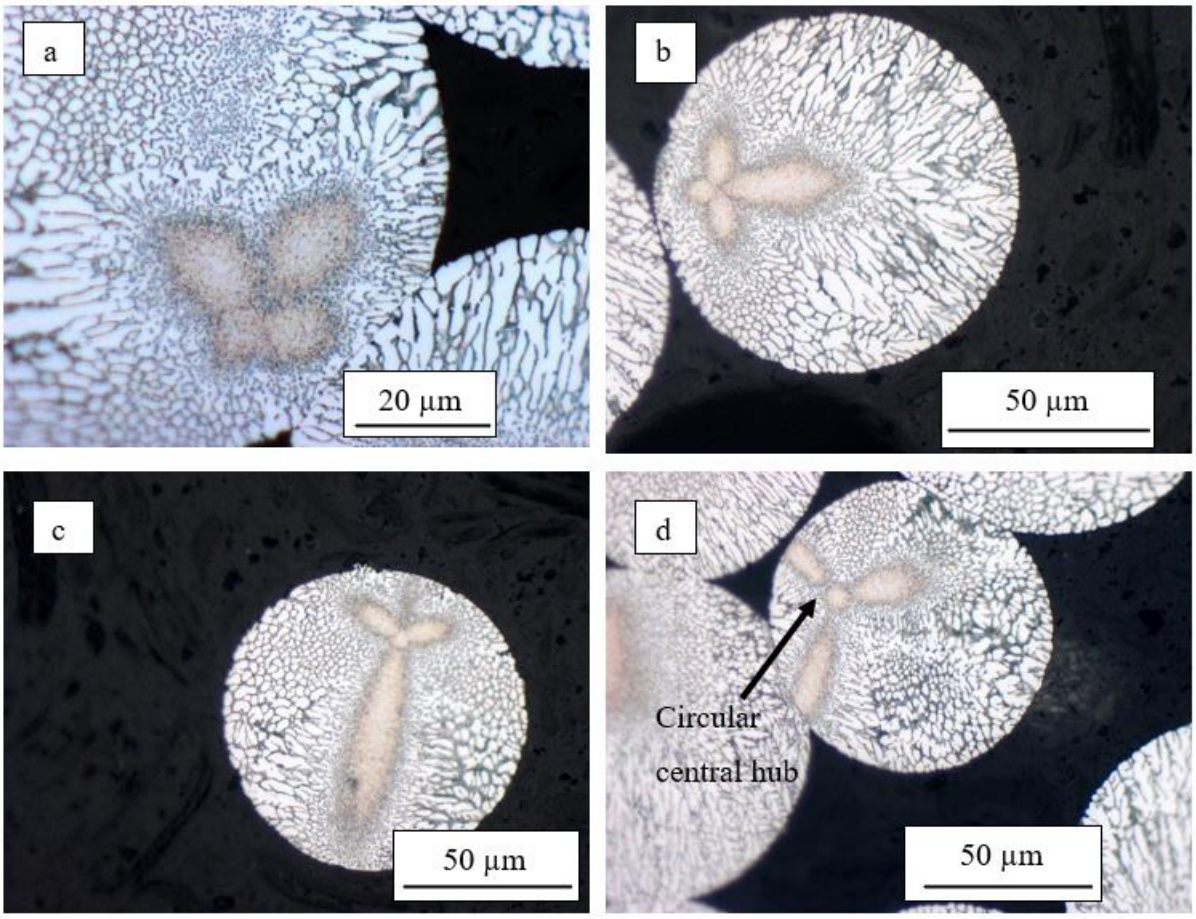
a
20 µm
b
50 µm
c
50 µm
d
Circular
central hub
50 µm

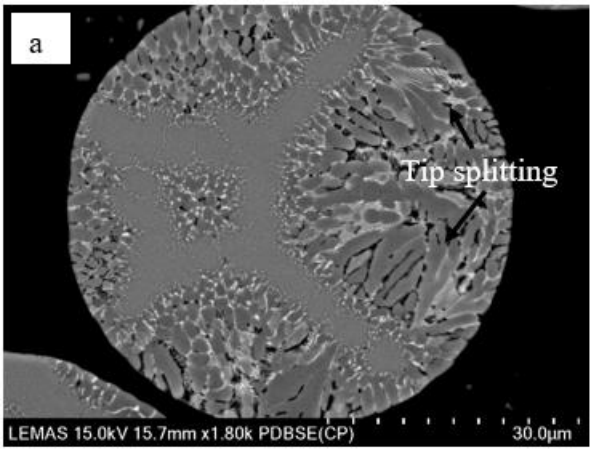
a
Tip splitting
LEMAS 15.0kV 15.7mm x1.80k PDBSE(CP)
30.0µm

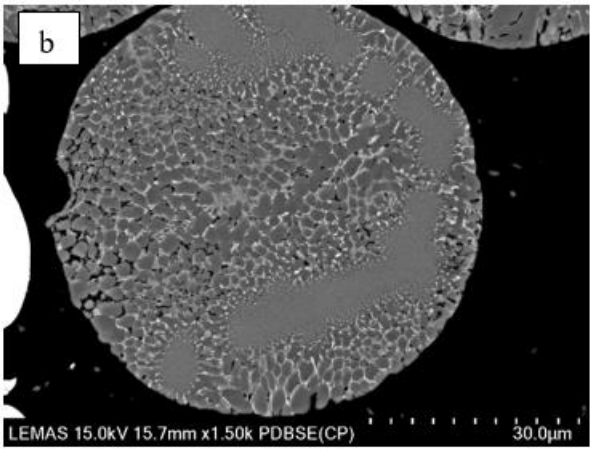
b
LEMAS 15.0kV 15.7mm x1.50k PDBSE(CP)
30.0µm

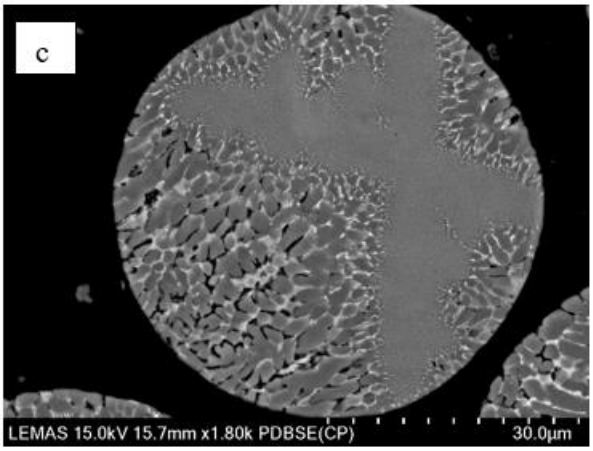
c
LEMAS 15.0kV 15.7mm x1.80k PDBSE(CP)
30.0µm

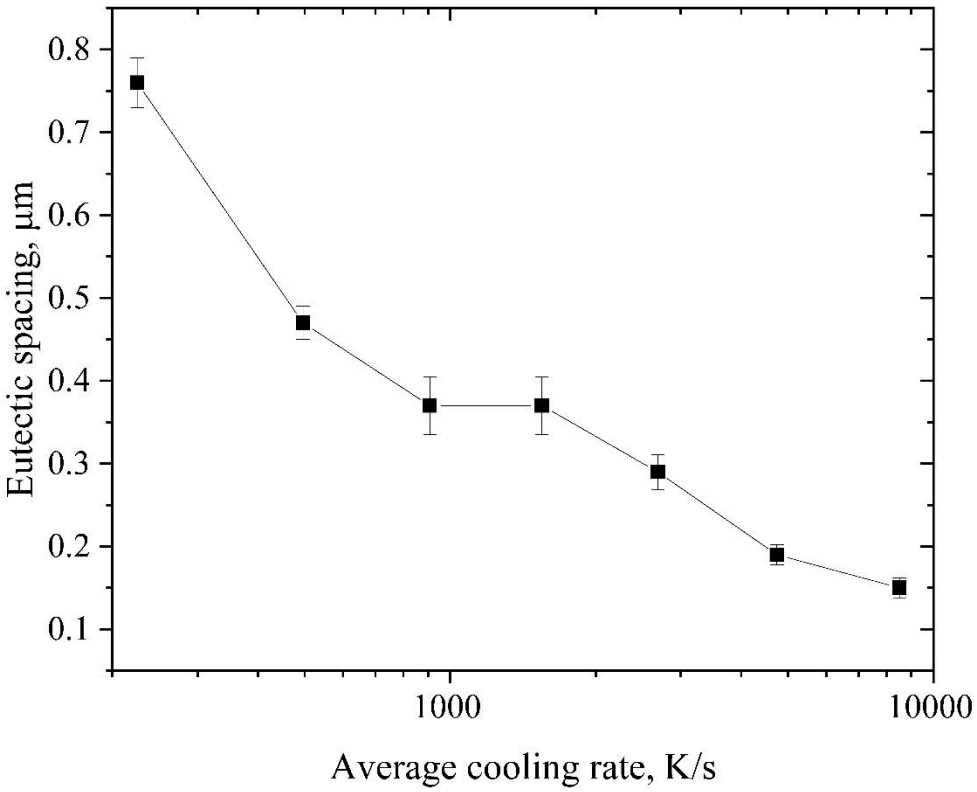
Eutectic spacing, µm
0.8
0.7
0.6
0.5
0.4
0.3
0.2
0.1
1000
10000
Average cooling rate, K/s

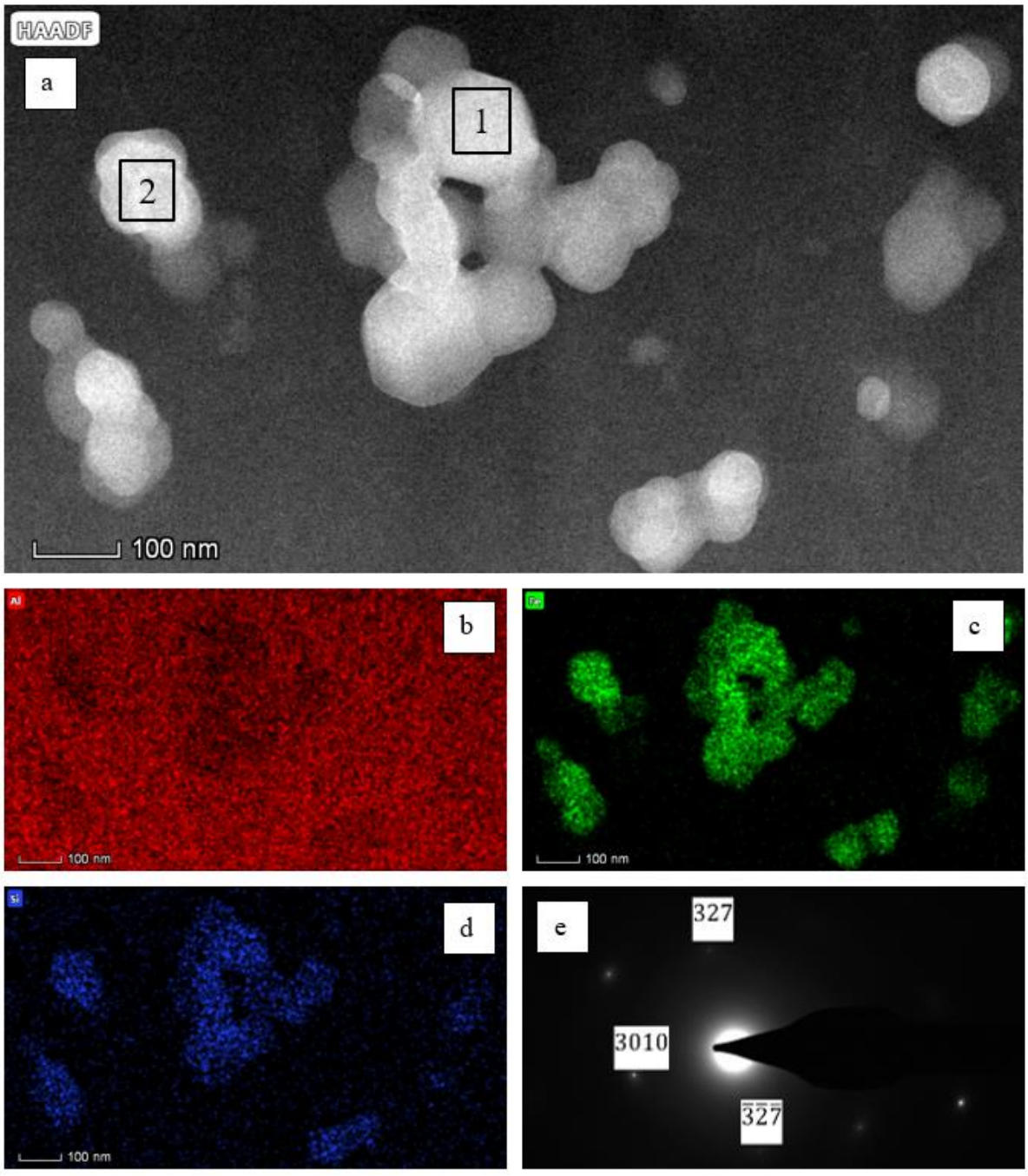
HAADF
a
1
2
100 nm
b
100 nm
c
100 nm
d
100 nm
e
327
3010
$\bar{3}\bar{2}\bar{7}$

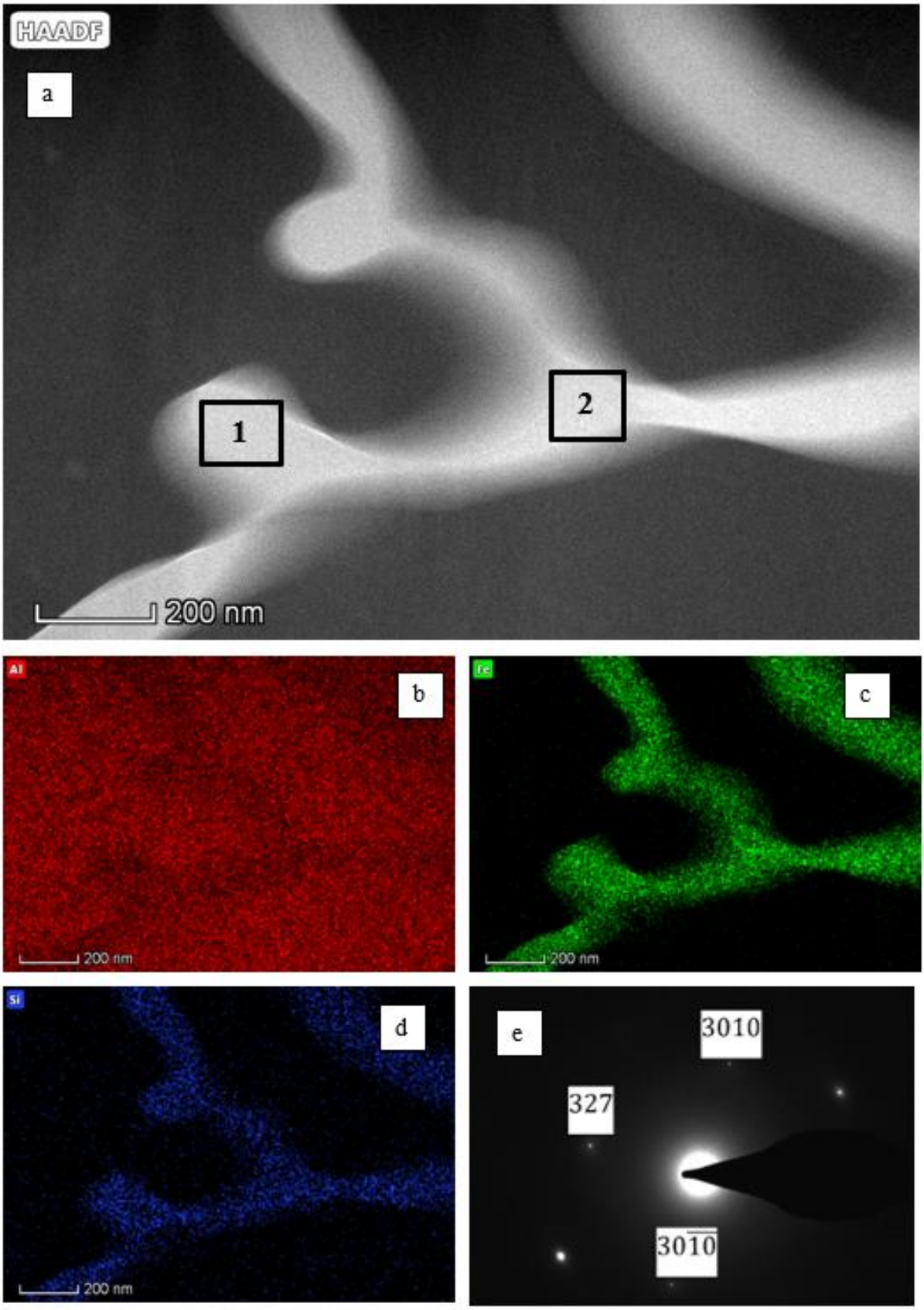
HAADF
a
1
2
200 nm
Al
b
200 nm
Fe
c
200 nm
Si
d
200 nm
e
3010
327
3010

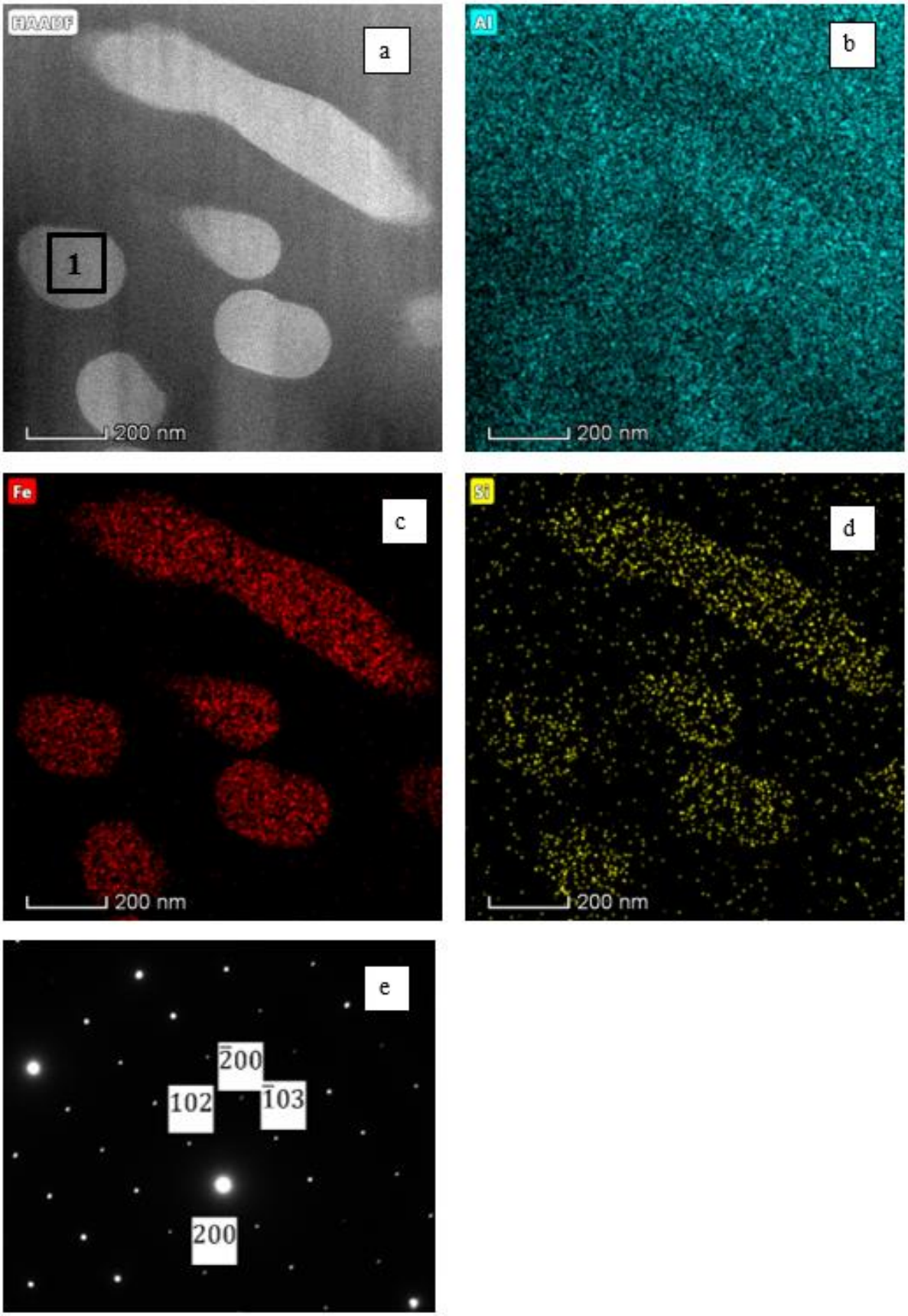
HAADF
a
1
200 nm
Al
b
200 nm
Fe
c
200 nm
Si
d
200 nm
e
$\bar{2}00$
102
$\bar{1}03$
200

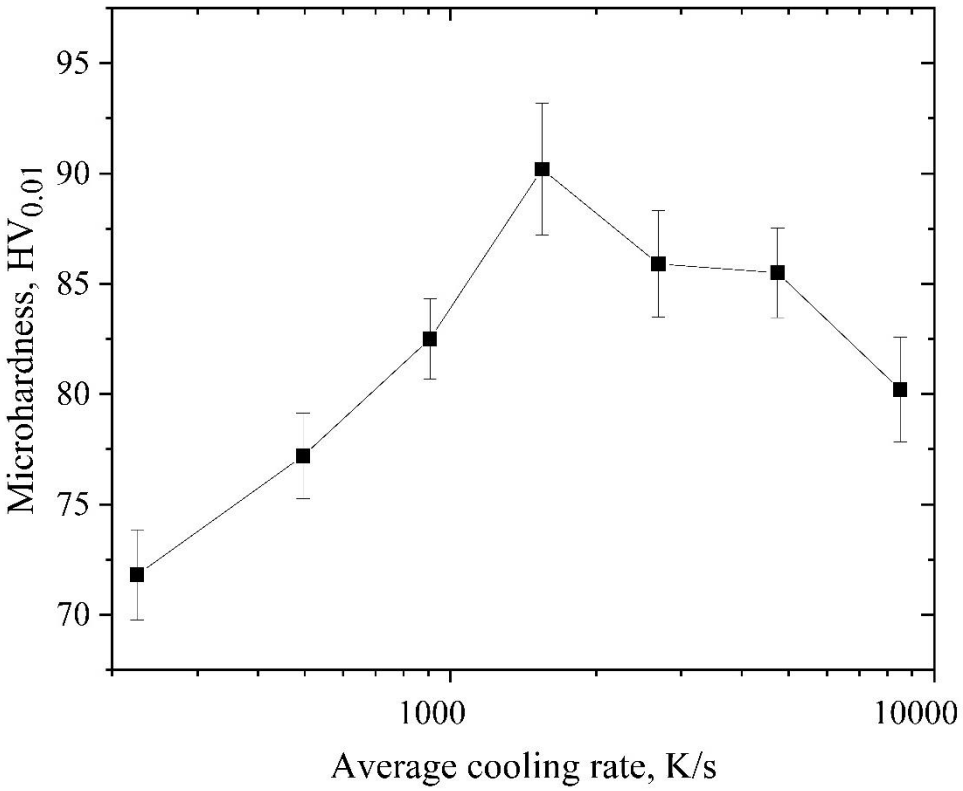
95
90
85
80
75
70
Microhardness, $HV_{0.01}$
1000
10000
Average cooling rate, K/s

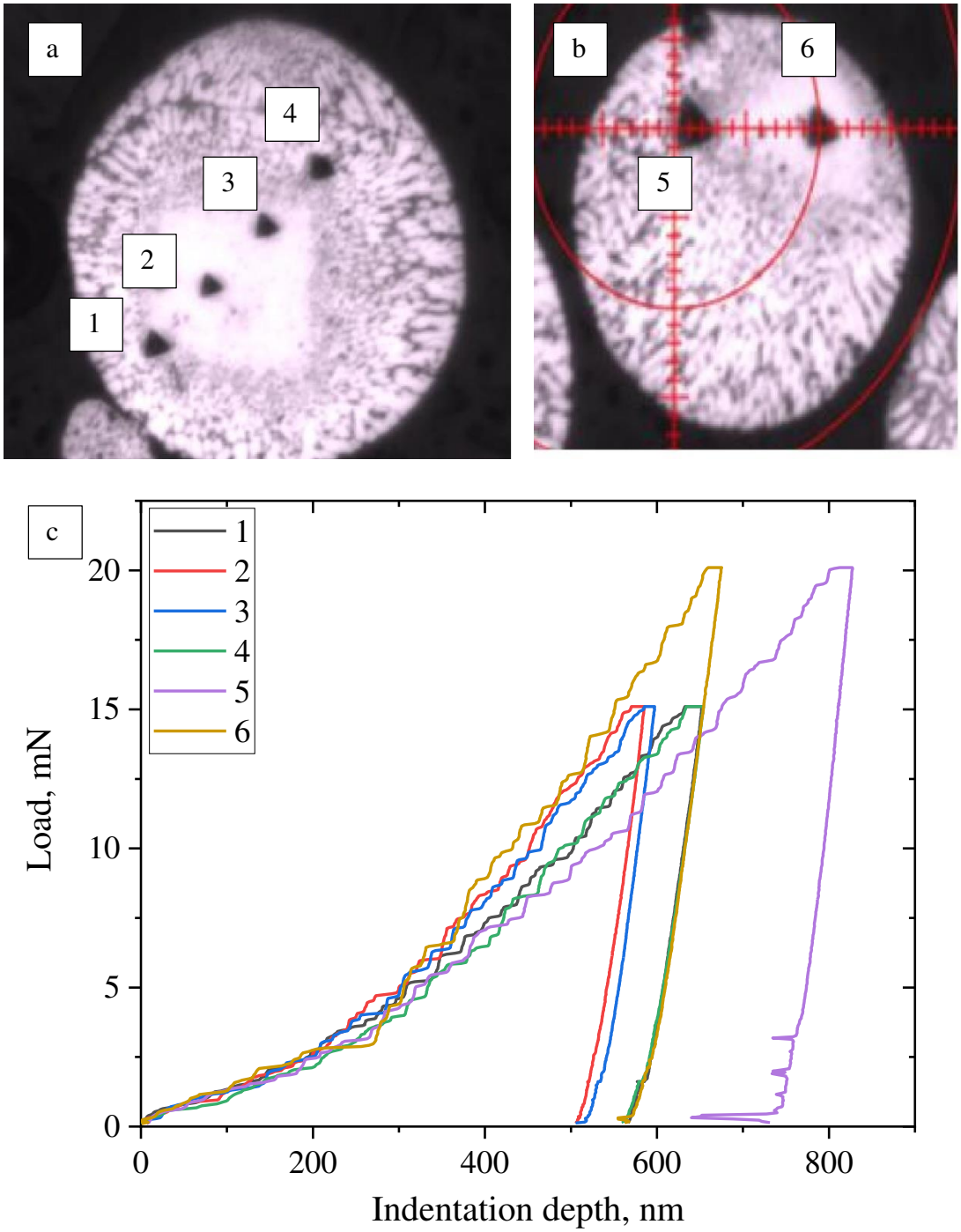
a
1
2
3
4
b
5
6
c
1
2
3
4
5
6
Load, mN
0
5
10
15
20
0
200
400
600
800
Indentation depth, nm